The growth and morphology of epitaxial multilayer graphene



2008 J. Phys.: Condens. Matter 20 323202

(http://iopscience.iop.org/0953-8984/20/32/323202)

IOP PUBLISHING JOURNAL OF PHYSICS: CONDENSED MATTER

J. Phys.: Condens. Matter **20** (2008) 323202 (27pp) doi:10.1088/0953-8984/20/32/323202

TOPICAL REVIEW

# The growth and morphology of epitaxial multilayer graphene

**J Hass, W A de Heer and E H Conrad**

The Georgia Institute of Technology, Atlanta, GA 30332-0430, USA

Received 24 March 2008
Published 18 July 2008
Online at stacks.iop.org/JPhysCM/20/323202

**Abstract**

The electronic properties of epitaxial graphene grown on SiC have shown its potential as a viable candidate for post-CMOS electronics. However, progress in this field requires a detailed understanding of both the structure and growth of epitaxial graphene. To that end, this review will focus on the current state of epitaxial graphene research as it relates to the structure of graphene grown on SiC. We pay particular attention to the similarity and differences between graphene growth on the two polar faces, (0001) and $(000\bar{1})$, of hexagonal SiC. Growth techniques, subsequent morphology and the structure of the graphene/SiC interface and graphene stacking order are reviewed and discussed. Where possible the relationship between film morphology and electronic properties will also be reviewed.

(Some figures in this article are in colour only in the electronic version)

## Contents



## 1. Introduction

Epitaxial graphene is a viable candidate for an all-carbon post-CMOS electronics revolution. This fact has provided an impetus for the study of epitaxial graphene and how it can be produced [1, 2]. The work stems from the attractive electronic properties of carbon nanotubes (CNTs) that have lead a variety of research efforts to develop CNT electronic switching devices. However, problems with large intrinsic resistance in contacts and the inability to control tube helicity (i.e. whether or not they are metallic or semiconducting) have made large scale integrated circuit designs problematic. A solution to these problems was proposed in 2001 when it was realized that similarities in the electronic and ballistic properties of graphene ribbons and CNTs could result in the development of epitaxial graphene electronics [1, 2]. Graphene nanoribbons can be considered as unrolled CNT but with different boundary conditions (two dimensional versus cyclic) [1, 3]. The advantage of graphene over CNTs for electronics resides in its planar 2D structure that enables circuit design with standard lithography techniques. This allows graphene to be cut with different shapes and selected edge direction. By tailoring the ribbon width it would be possible to design semiconductor graphene ribbons with a tunable band gap [3–5].

Research into the electronic properties of graphene has followed two parallel courses. One course involves the study of mechanically exfoliated graphene sheets [6–9]. In this research graphene flakes (typically micron size) are mechanically peeled from a bulk graphite crystal onto a support substrate. Once a single graphene sheet is subsequently

 

located by optical microscopy, metal contacts are attached for transport studies [7–13]. In the second research avenue graphene is directly grown on large area insulating or semiconducting substrates. Once grown, the films are lithographically patterned and metal contacts applied to make electronic devices [1, 2, 14, 15]. Graphene produced in this way is referred to as epitaxial graphene (EG). Mechanically exfoliated graphene flakes have been used to study a variety of fundamental graphene properties. These flakes have been shown to exhibit 2D transport properties characteristic of the chiral massless Dirac electrons [16] expected for an isolated graphene sheet. These include an unusual half-integer quantum Hall effect and a non-zero Berry's phase [7, 8]. What has propelled epitaxial graphene research as a leading contender for post-CMOS electronics was the discovery that even multilayer graphene films grown on SiC show electronic properties similar to an isolated graphene sheet. These include a Berry's phase of $\pi$, weak anti-localization, and a square root dependence of the Landau level energies with applied magnetic field [2, 14, 15, 17, 18].

The similarity of EG or exfoliated graphene's transport properties to the transport properties of a theoretically isolated graphene sheet is remarkable, considering that graphene/substrate interactions should influence the 2D Dirac electrons responsible for graphene's unusual properties. On the other hand the result is very fortuitous since graphene grown on an insulating substrate promises the most practical and scalable approach to 2D graphene electronics. For this reason graphene grown on SiC has been the focus of research targeting a path towards graphene electronics.

In addition to research demonstrating the transport properties of graphene grown from SiC, parallel research efforts have been searching for a structural explanation of why epitaxial graphene behaves like an isolated graphene sheet [19–26]. While these fundamental studies continue, research on the growth kinetics of epitaxial graphene has just begun [27, 28]. The impetus for the latter work is much the same as in the infancy of Si-based electronics where integrated circuits were not developed until nearly a decade after the invention of the transistor. This lag was due to the inability to produce the high quality wafer-scale Si substrates necessary for improvements in Si-based electronic devices. Likewise, the viability of graphene electronics rests on the ability to make wafer-scale graphene with controlled thickness and specified crystallographic orientation so that electronic properties can be reproducibly tailored. This goal is now being realized. Hundreds of gated epitaxial graphene devices with similar switching properties have been fabricated on a single graphene/SiC chip [29].

In this review we will outline the current state of epitaxial graphene research. This includes a review of the structure and a comparison of the electronic properties of graphene and graphite in section 2. Because SiC is currently the primary substrate for growing EG, we will also review its structure in section 2. As mentioned above, moving graphene electronics forward requires the ability to produce and integrate large graphene sheets onto semiconducting or insulating substrates. We therefore review the current progress in growing graphene on SiC in section 3. Because SiC is bipolar, we compare growth modes on both polar faces of SiC. It must be emphasized that there are significant differences in both the growth and the structure of graphene on the two polar faces. These differences are often overlooked in the literature. In this review we will pay specific attention to this detail because subsequent electronic and transport properties on the two polar surfaces are related to these differences. For completeness, we also include a brief discussion of exfoliated graphene in section 3 with the intent of making realistic comparisons of the structural order of these films with epitaxial graphene. In section 4 we review the structure and epitaxy of graphene grown on SiC. This includes a comparison of what is known about the graphene/substrate structure and interactions as well as graphene stacking on both SiC polar faces. We also present a brief look at how EG thickness is determined.

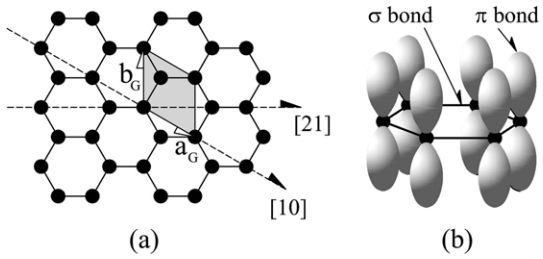


**Figure 1.** (a) Graphene hexagonal structure of identical carbon atoms. The unit cell (shaded) containing two carbon atoms is shown along with standard unit cell vectors $\mathbf{a}_G$ and $\mathbf{b}_G$. The 'armchair' edge and the 'zig-zag' directions are shown ([21] and [10] respectively). (b) Schematic of the in-plane $\sigma$ bonds and the $\pi$ orbitals perpendicular to the plane of the sheets.

## 2. Graphene and SiC structure

### *2.1. Graphene structure*

Graphene can be defined structurally or electronically. For the purpose of this review we will use a structural definition of graphene regardless of its stacking. At the same time we must keep in mind that the unique electronic properties of graphene refer to those from an electronically isolated graphene sheet and that the electronic properties of both epitaxial and exfoliated graphene are not necessarily those of an isolated sheet. With this proviso we define graphene as a single two dimensional hexagonal sheet of carbon atoms as shown in figure 1(a). The standard in-plane unit cell vectors are $|\mathbf{a}_G| = |\mathbf{b}_G| = 2.4589$ Å [30]. The unit cell contains 2 carbon atoms at (0, 0) and $(a_G/3, 2b_G/3)$. This gives a carbon areal density of 3.820 atoms Å$^{-2}$.

Graphene bonds are hybridized into a $sp^2$ configuration. There are three in-plane ($\sigma$) bonds/atom. These bonds are extremely strong and form the rigid backbone of the hexagonal structure. It is the partially filled $p_z$ orbitals ($\pi$ orbitals) perpendicular to the plane that are responsible for the electron conduction (see figure 1(b)). Because of the out-of-plane $\pi$ orbitals, interactions between graphene and a substrate or between graphene layers should influence the electronic

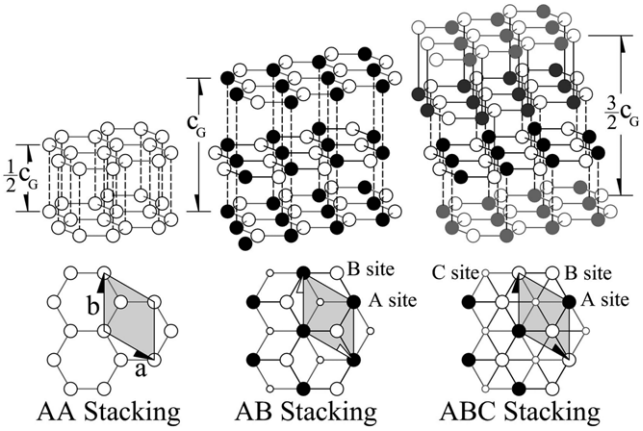


**Figure 2.** Three common graphite structures with different graphene stacking arrangements: (i) Hexagonal AA . . . stacking, (ii) Bernal AB . . . stacking and (iii) rhombohedral ABC . . . stacking. Shaded areas are the unit cells.

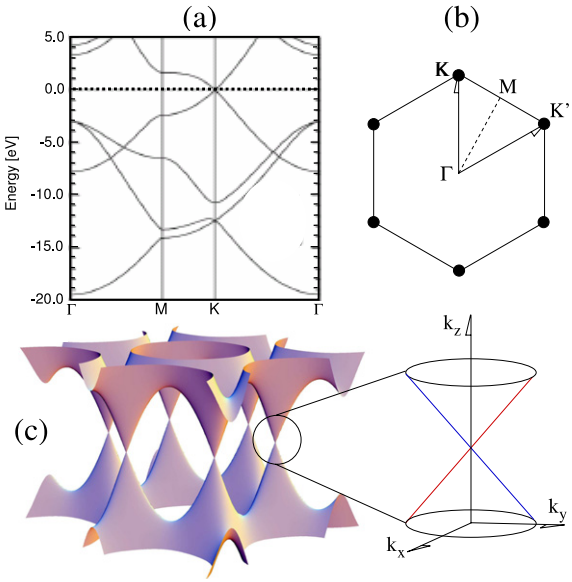


**Figure 3.** (a) An *ab initio* band structure calculation of graphene from [35] (b) a schematic of the Fermi surface of graphene consisting of points intersecting the Dirac cone. (c) The two dimensional tight binding energy surface of graphene. The blow up shows the linear dispersion (Dirac cones) near the K-point in the vicinity of $E = E_F$.[1]

structure of epitaxial or exfoliated graphene. The fact that the transport properties of exfoliated flakes or single and multilayer epitaxial graphene grown on SiC are so similar to a theoretical isolated graphene sheet, despite substrate or layer interactions, requires an explanation that will be discussed in detail in section 4.

Sheets of graphene are known to stack in a number of ways to produce materials with the generic name of graphite. The three most common stacking arrangements are: hexagonal or AA . . . stacking, Bernal or AB . . . stacking and rhombohedral or ABC . . . stacking (see figure 2). The lowest energy stacking and most abundant form (80%) in single crystal graphite is Bernal stacking [31]. The Bernal structure is formed by stacking two graphene sheets on top of each other and rotating one 60° relative to the other about a $z$ axis (in the $\widehat{\mathbf{c}}$ direction through any atom). The sheets are separated by a distance $c_G/2$ where $c_G = 6.672$ Å at 4.2 K and 6.708 Å at 297 K [30]. This produces two sublattices of atoms, an A atom positioned above an A atom in the sheet below or a B atom with no atom below it in the adjacent sheet. The Bernal cell has 4 atoms/cell. In Bernal graphite the overlap of partially filled $p_z$ orbitals ($\pi$ orbitals) perpendicular to the plane account for the weak bonding between AB . . . sheets. These bonds are sometimes referred to as van der Waals bonds [32]. Hexagonal AA . . . stacking consists of two unrotated sheets separated by a distance $c_G/2$ perpendicular to the sheets (figure 2). This is the least common form of graphite (<6%). It contains a single sublattice with 2 atoms/cell. Rhombohedral graphite, which accounts for 14% of natural graphite [31], is formed with three graphene sheets each separated by $c_G/2$ (see figure 2). The second sheet is rotated relative to the first by 60° as in Bernal graphite. The third sheet has the same orientation relative to the second but is translated $(2a_G/3, b_G/2)$ from the second sheet. The rhombohedral cell has 6 atoms. Note that that $c_G/2$ in figure 2 is slightly different for each stacking arrangement. However, these differences are $\lesssim$0.2% [33] of Bernal stacking and can usually be ignored.

The electronic band structure of graphene was first calculated by Wallace as early as 1947 [34]. Figure 3(a) shows an *ab initio* band structure calculation for an isolated graphene sheet. The crucial aspect of the band structure occurs at $E_F$ ($E = 0$ in the plot) with an electron momentum near the K- or K′-point. Hopping between the two equivalent carbon sublattices A and B (see figure 1) leads to the $\pi$ bands intersecting at the zone boundary, 'K-point' [36]. These intersection points are known as Dirac points. The energy dispersion near the Dirac points is linear; $E = \hbar k v_F$ where $v_F \approx c/300$ ($c$ is the speed of light) and gives rise to a Fermi surface near $E = 0$ that is composed of the six Dirac cones in figures 3(b) and (c). This unique linear dispersion means that the effective mass of the electrons is zero near $E_F$.

The linear dispersion has another important consequence on the electron states below $E_F$ and the hole states above $E_F$. Electrons and holes cannot be described by independent Schrödinger equations. Instead the electrons and holes are represented as quasi-particles connected in a way that is best described by the Dirac equation [37–45]. Electrons and holes belonging to the same branch of the dispersion curve are described by a pseudospin $\sigma$ that is parallel to the electron momentum, but opposite the hole momentum. This 'chirality' means that an electron hopping from K to K′ (see figure 3(b)) is not allowed since the pseudospin is not conserved. This conservation rule gives rise to the ballistic transport observed in graphene and CNTs [16, 46]. As in CNTs, electron phonon scattering is expected to be very weak [46, 47]. This coupled with the fact that long range Coulomb potentials cannot trap Dirac quasi-particles [48, 49] means that coherence lengths can be very large in epitaxial graphene [2]. For a detailed theoretical treatment the reader is referred to [36].

[1] We thank G M Rutter for supplying the results of his tight binding calculation.

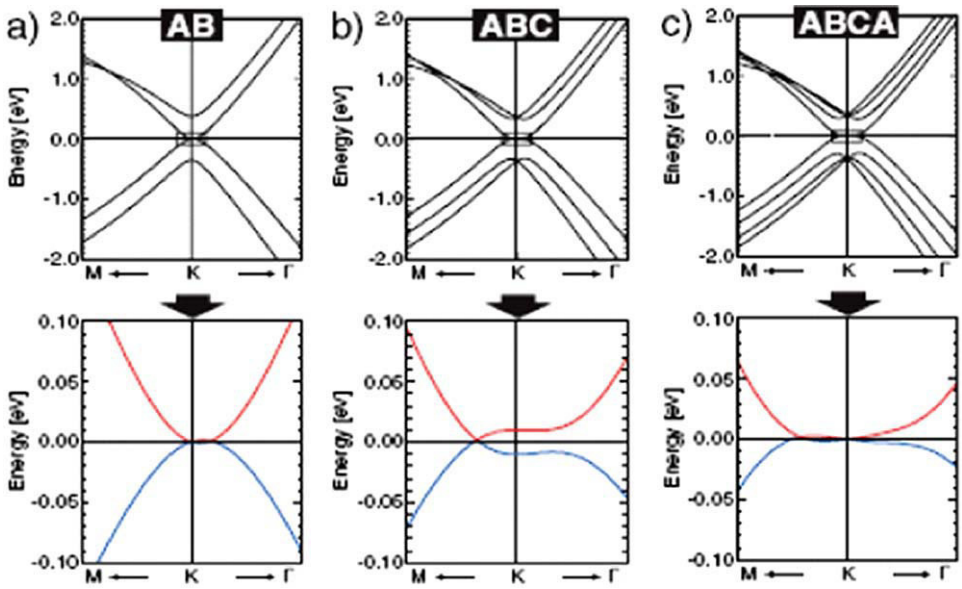


**Figure 4.** *Ab initio* band structures near the K-point for different graphene stacking arrangements. (a) An AB . . . stacked graphene pair, (b) three ABC . . . stacked graphene sheets and (c) four ABCA . . . stacked graphene sheets. Bottom panels are blowups of the band crossings near $E = E_F$. Reproduced with permission from [35]. Copyright 2006 by the American Physical Society.

The fundamental properties of graphene discussed above are altered when the equivalence of the A and B sublattices is broken. This can occur in many ways. For instance, in thin ribbons of graphene the edge structure becomes important. A ribbon width dependent gap opens at $E_F$ that depends on the details of the ribbon edge geometry and termination [3, 4, 50, 51]. Graphene ribbons with 'armchair' edges running in the [21] direction in figure 1 contains both A and B sites on the edge while the 'zig-zag' edges running in the [10] direction contains either all A or all B sites. A 'zig-zag' ribbon is metallic and the 'armchair' ribbon is semiconducting with a ribbon width dependent band gap.

The stacking sequence of graphene layers can also significantly alter the band structure by breaking the A and B sublattice symmetry [35, 41, 42, 45]. While AA . . . stacking, of graphene sheets preserves the symmetry, AB . . . stacking does not. In AB . . . stacking the A atoms are bonded to A atoms in the plane above while B atoms have no corresponding atom in the plane above (see figure 2). The effects of these different stacking patterns on the band structure of multilayer graphene are demonstrated in figure 4. In both Bernal and rhombohedral stacking the weak inter-planar interaction breaks the AB . . . symmetry and produces bonding $\pi$ and $\sigma$ states and anti-bonding $\pi^*$ and $\sigma^*$ states resulting in a splitting of the bands near the Dirac point and a corresponding change in energy dispersion that is no longer linear.

### 2.2. SiC structure

Since the vast majority of research on EG has focused on graphene grown on SiC, it is worth reviewing the SiC structure. This is particularly true of its surface structure since the growth of EG is highly dependent on which SiC face it is grown. SiC grows in both cubic and a number of hexagonal polytypes. Most graphene growth on SiC has focused on the hexagonal form. The two commonly used polytypes of hexagonal SiC are 6H and 4H. Their unit cells are shown in figure 5. In both cases the cells are composed of Si–C bilayers with different stacking arrangements. For 4H-SiC the stacking is ABCB . . . and for 6H-SiC it is ABCACB . . .. The $c_{SiC}$ and $a_{SiC}$ spacings of the 4H and 6H unit cells are given in table 1. An $n$H–SiC cell is made of $n$ SiC bilayers. Each bilayer contains a plane of C atoms and a plane of Si atoms. For reference in later sections we define a relative areal density of carbon or silicon atoms, $\rho$, to be 1 in a bilayer plane (the atom density in a bilayer is therefore $\rho = 2$). The ideal distance between bilayers for $n$H–SiC is $(3/4)(1/n)c_{SiC}$ and the Si–C bond length is $(1/4)(1/n)c_{SiC}$. There are small vertical relaxations from these ideal spacings that are of the order $10^{-4}c_{SiC}$ [53]. For the purpose of graphene growth on SiC, these small relaxations can be ignored.

**Table 1.** Structural parameters of 4H- and 6H-SiC from [52].

| SiC polytype | $a_{SiC}$ (Å) | $c_{SiC}$ (Å) |
|---|---|---|
| 4H | 3.0805 | 10.0848 |
| 6H | 3.0813 | 15.1198 |

It is important to realize that SiC has two polar faces perpendicular to the $c$-axis. The bulk terminated SiC(0001) Si-terminated face (Si-face) has one dangling Si bond/Si atom, while the SiC(000$\bar{1}$) C-terminated face (C-face) has one C dangling bond per C atom (see figure 5). As we will demonstrate in sections 3 and 4 both the growth of graphene and its structure are very different on these two polar faces.

### 2.3. Epitaxy of graphene on SiC

Because of the relationship between graphene and SiC lattice constants, there are a large number of possible orientations of

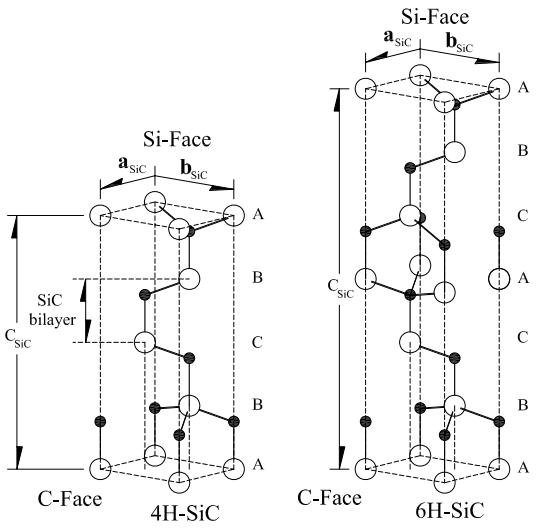


**Figure 5.** The unit cell structure of 4H- and 6H-SiC. Filled circles are carbon atoms and open circles are silicon atoms.

a graphene lattice that lead to nearly commensurate structures with the SiC(0001) and $(000\bar{1})$ surfaces. Many of these structures are observed in the graphene/SiC system. Which of these structures form depends on the specific SiC polar face chosen for growth along with other experimental conditions. Therefore, we present these structures in this section as a reference for future discussions. Since we will be dealing with both graphene and SiC basis vectors, we will need to switch between notation to describe the surface periodicity of various supercells. To avoid confusion we will write the periodic supercells in graphene basis vectors with the subscript $G$, i.e. $(n \times m)_{\mathrm{G}}$. Cells in the SiC basis vectors will not be subscripted.

In general these commensurate phases can be calculated when an integer multiple of the SiC unit cell is nearly equal to an integer multiple of the graphene unit cell;

$$\left|n'\mathbf{a}_{\mathrm{SiC}} + m'\mathbf{b}_{\mathrm{SiC}}\right| \approx \left|n\mathbf{a}_{\mathrm{G}} + m\mathbf{b}_{\mathrm{G}}\right|, \tag{1}$$

where $n'$, $m'$, $n$ and $m$ are integers. For convenience we define the dimensionless distances $R_{\mathrm{G}} = \sqrt{m^2 + n^2 - nm}$.

In terms of SiC unit vectors, a set of commensurate structures gives rise to both $(l \times l)$ and $(l\sqrt{3} \times l\sqrt{3})$R30 SiC reconstructions when:

$$l \approx \text{Integer} \begin{cases} \dfrac{a_{\mathrm{G}}}{a_{\mathrm{SiC}}} R_{\mathrm{G}} & (l \times l) \\ \dfrac{a_{\mathrm{G}}}{a_{\mathrm{SiC}}\sqrt{3}} R_{\mathrm{G}} & (l\sqrt{3} \times l\sqrt{3})\mathrm{R30}. \end{cases} \tag{2}$$

The rotation angle of the commensurate graphene sheets, relative to the SiC $n'\mathbf{a}_{\mathrm{SiC}}$ direction, can be calculated for different integer $m$ and $n$'s:

$$\theta(\mathrm{mod}\ 60^\circ) = \begin{cases} \cos^{-1}\left(\dfrac{2m-n}{2R_{\mathrm{G}}}\right) & (l \times l) \\ \cos^{-1}\left(\dfrac{2m-n}{2R_{\mathrm{G}}}\right) - 30 & (l\sqrt{3} \times l\sqrt{3})\mathrm{R30}. \end{cases} \tag{3}$$

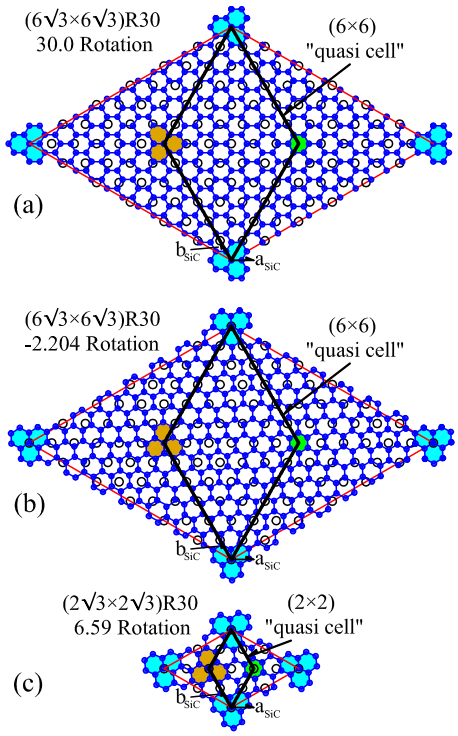


**Figure 6.** (a) and (b) are two graphene–SiC $(6\sqrt{3} \times 6\sqrt{3})$R30 unit cells, one with graphene rotated 30° and the other with graphene rotated −2.204° relative to the SiC unit cell (red/light grey line). Open circles are atoms in the SiC and filled circles are C atoms in the graphene layer. The shaded area shows high symmetry points between the graphene lattice and the SiC lattice. A $(6 \times 6)$ unit cell connecting the high symmetry points is also shown. (c) A $(2\sqrt{3} \times 2\sqrt{3})$R30 cell with graphene rotated 6.59° is also shown with its quasi-$(2 \times 2)$ cell.

One structure of particular relevance is the $(6\sqrt{3} \times 6\sqrt{3})$R30 structure that is the predominant reconstruction observed by low energy electron diffraction (LEED) for graphene grown on the Si-face of SiC [54–56]. A ball model of this commensurate graphene structure is shown in figure 6. Note the high symmetry points of the graphene lattice relative to the SiC (shaded hexagons). These are points where either a carbon atom in the graphene layer sits directly above an atom in the SiC layer below, or that a SiC atom lies directly below the center of a graphene hexagon. We can define a quasi-unit-cell that is defined by these high symmetry points. For the commensurate $(6\sqrt{3} \times 6\sqrt{3})$R30 structure shown in figure 6 the quasi-cell would be a $(6 \times 6)$ SiC unit cell. Many of the nearly commensurate graphene/SiC structures have these high symmetry sites that lead to smaller quasi-cells. These cells are mentioned because, as we will see in sections 3 and 4.1, the influence of the SiC substrate/graphene interaction and the graphene–SiC interface structure causes an apparent distortion of the first 1–2 graphene layers so that scanning tunneling microscopy (STM) images often see a surface unit cell that is smaller than the cell measured by diffraction.

Table 2 is a short list of these commensurate graphene/SiC structures showing the graphene sheet's rotational angle relative to the SiC$[00\bar{1}0]$ direction along with their relative strain. The strain is defined as $\Delta l/l = 1 - (a_{\mathrm{G}}/a_{\mathrm{SiC}})R_{\mathrm{G}}/l$ or

**Table 2.** A short list of graphene/SiC commensurate structures.

| Commensurate SiC unit cell | Graphene angle relative to SiC[00$\bar{1}$0] | Strain $\Delta l/l$ (%) | Ref. |
|---|---|---|---|
| $(6\sqrt{3} \times 6\sqrt{3})$R30 Quasi $(6 \times 6)$ | 30° | 0.15 | [54–56] |
| $(6\sqrt{3} \times 6\sqrt{3})$R30 Quasi $(6 \times 6)$ | ±2.204° | 0.15 | [129] |
| $(9 \times 9)$ Quasi $(3\sqrt{3} \times 3\sqrt{3})$ | $30 \pm 2.543°$ | 0.05 | [55, 59] |
| $(5 \times 5)$ | ±16.10° | −0.30 | [55, 86] |
| $(2\sqrt{3} \times 2\sqrt{3})$R30 Quasi $(2 \times 2)$ | ±6.59° | 0.44 | [55, 71] |

$1-(a_G/\sqrt{3}a_{SiC})R_G/l$ for the $(l \times l)$ and $(l\sqrt{3} \times l\sqrt{3})$R30 cells, respectively. These nearly commensurate structures represent a fraction of the structures possible but are important in that they have been observed in various experiments. A larger group of rotational phases observed for graphene grown on the C-face of SiC will be discussed in section 4.2. The quasi-cells, if they exist, are also listed alongside the commensurate structures in table 2.

## 3. Epitaxial graphene production

In this section we will review the status of research on the production of epitaxial graphene grown from hexagonal 4H- and 6H-SiC. While these substrates represent the bulk of epitaxial graphene research, work on metal surface graphitization continues [57, 58] and shows some promise. We again emphasize that the graphitization and the subsequent morphology and electronic properties of epitaxial graphene depends strongly on which of the two polar faces they are grown. We begin this section with a brief history of graphene growth on SiC, a summary of common sample preparation techniques, some important structural considerations and a discussion of what is and is not known about the growth kinetics.

The pioneering investigations into graphite formation on 6H-SiC(0001) and (000$\bar{1}$) surfaces were performed by van Bommel *et al* [54]. They showed that heating either the C-face or the Si-face surfaces in ultrahigh vacuum (UHV) to temperatures between $1000\,°C \lesssim T \lesssim 1500\,°C$ sublimated sufficient Si to leave behind a carbon rich surface. LEED patterns from these surfaces were consistent with a surface graphite structure. They also found a corresponding change in the carbon Auger peak from a 'carbide' character to a 'graphite' character. Subsequent work showed that that the carbon layers at these temperatures ordered into a graphene structure with clear $sp^2$ bonding that was aligned with the SiC substrate [54–56, 59–67]. It was also clear from these early works that graphene formation on the two polar surfaces was clearly different [54, 56, 60–62]. Graphene growth on the Si-face is much slower compared to growth on the C-face [60, 68]. In addition, Si-face graphene is epitaxial with an orientational phase rotated 30° relative to the SiC while C-face films can have multiple orientational phases [54, 62]. Because of the orientational disorder in C-face grown graphene, most structural, growth and electronic studies of epitaxial graphene focused on Si-face graphene. We will see in section 3.3 that new research has shown that the quality of C-face graphene is far superior to that grown on the Si-face. In fact, improvements in growth already allow device integration over hundreds of microns.

It should be noted at this point that absolute temperature measurements of SiC near the graphitization temperature are very difficult. Because SiC is transparent, radiative light from sample holders though the SiC makes infrared and optical pyrometer methods prone to absolute errors. Likewise eutectic formation of SiC with the standard W–Re thermocouple material requires the thermocouple junction to be near but not on the sample. For temperatures near and above 1200 °C thermal gradients on sample holders can easily lead to absolute temperature errors of 50–100 °C from one experimental group to another.

From stoichiometry alone the formation of a single graphene sheet requires the carbon contained in 3.14 SiC bilayers $(2/a_G^2)/(1/a_{SiC}^2) = 3.139$. Liberating this much carbon requires the removal, and subsequent sublimation into the vacuum, of Si from more than three SiC bilayers. This presents a serious challenge because even at temperatures of 1440 °C (well above the graphitization temperature), the diffusion of Si or C in bulk SiC is essentially zero [69, 70].

Another stoichiometric consequence of the SiC bilayer carbon concentration is that when Si is removed from the SiC/graphene interface, so that enough carbon has been liberated to form a single graphene sheet, there must be a partial SiC bilayer left at the carbon–graphene interface. We can define the 'excess carbon' remaining in the partial SiC bilayer as the amount of surface carbon atoms/((1 × 1) SiC cell) after the $n$th graphene layer has formed but before enough carbon is available to complete the $n$th + 1 layer. In other words, we are assuming that a graphene layer forms only when the areal density of carbon is equal to the areal density of graphene. While this is obviously not the case since partial graphene layers do form, the 'excess carbon' parameter allows us to view the amount of partial SiC bilayers remaining after the completion of an integer number of graphene layers has formed (assuming all the carbon comes from the SiC substrate). A plot of the excess carbon as a function of SiC bilayers consumed during Si sublimation reveals a periodic minimum every ∼7 graphene layers. This is demonstrated in figure 7. The role of this carbon is unclear. It must play a role in the growth kinetics by affecting the diffusion of Si through the bulk/graphene interface. Because of the bonding symmetry differences on the two polar faces, it is expected that the release of Si on these two faces must also be different. Also, since a partial SiC bilayer leads to steps on the surface, achieving a smooth graphene layer-by-layer growth becomes a problem unless the partial bilayers can be removed by some process.

### 3.1. SiC surface preparation

Because of the interest in SiC as a wide gap semiconductor, a great deal of literature exists on both its bulk and surface

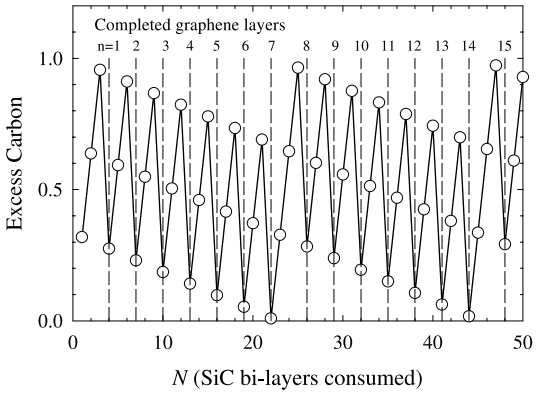


**Figure 7.** Excess carbon versus the number of SiC bilayers that have been completely depleted of Si. Dashed lines indicate the number $n$ of integer graphene layers that have been formed after sublimating $N$ SiC bilayers.

structure. For reviews the reader is referred to [71] and [72]. The relevance of any initial SiC surface preparation techniques to epitaxial graphene growth has yet to be proven. This is because earlier SiC surface studies were concerned with producing ordered SiC surfaces with specific structural and chemical stoichiometry. The massive material transport and rearrangement of many SiC bilayers involved at the high temperatures during graphitization make the influence of the details of the starting surface questionable. Claims that certain surface preparation techniques or pre-graphitization SiC surfaces lead to better graphene order have not been substantiated. We begin by first reviewing these pre-treatments. Since the effects of these pre-cleaning stages and the resulting series of reconstructions that follow are specific to the two polar faces of SiC, their influence on the graphitization process will be discussed for the Si-face and C-face separately.

In earlier studies high quality commercial substrates were not available. Macroscopic surface disorder was treated by dry oxidation for up to 3 h at 1100 °C followed by HF etching [71, 73]. Current studies use high quality commercial SiC samples[2] and these cleaning techniques are no longer used. Even so, surface scratches from polishing remain even in the highest grade SiC wafers. To remove these scratches the samples are hydrogen-etched. This procedure starts by ultrasonic precleaning in acetone and ethanol, followed by hydrogen etching procedures that are listed in the literature [74, 75]. The samples are usually etched in a furnace atmosphere of 5% $H_2$ and 95% Ar mixture at 1 atm pressure, although *in situ* UHV $H_2$ plasma beam etching has also been studied [65]. The latter technique gives rise to a higher substrate roughness. A general furnace hydrogen etching cycle consists of ramping to between 1500–1600 °C at a rate of 100 °C $min^{-1}$ followed by a 30 min soak at 1600 °C. The sample is then cooled at a rate ∼50 °C $min^{-1}$ down to 800 °C and allowed to cool rapidly down to room temperature. It is important that the samples are cooled slowly after the maximum temperature to remove the crystallized Si deposits produced during etching [76]. The $H_2$ etching treatment leaves a regular atomic stepped surface. The step density is determined only by the original sample miscut with the step height usually one unit cell high. Typically terrace widths exceed many microns.

Once $H_2$ etched, there still remains a problem with surface oxides. Heating the samples to 950–1100 °C for 6 min in UHV will remove the surface oxide by the formation of SiO gas. This means that the oxide removal also depletes the Si surface concentration. To get around this problem samples can be heated in the presence of a Si flux (∼$10^{14}$ $cm^{-2}$ $s^{-1}$ for ∼2 min) to remove oxides while preserving the surface chemical stoichiometry. [59, 62, 77, 78] The sample temperature must be kept above 850 °C in the presence of the Si flux to prevent the formation of a polycrystalline Si surface and no higher than 900–1000 °C to prevent etching. Note that this process allows the removal of $O_2$ at a much lower temperature than by simply heating. Kaplan and Parrill have also used a 0.1–1.0 monolayer $s^{-1}$ Ga flux at 800–1000 °C to achieve similar results [73]. It was also noted that at least two types of oxides were present on the surface. The most persistent oxide requires more time or a higher temperature to remove. The amount of this oxide was correlated to the degree of surface roughness [73].

### 3.2. Si-face graphene production

*3.2.1. Si-face pre-graphitization.* Prior to the formation of graphene, the SiC(0001) Si-face surface goes through a number of surface reconstructions depending on the surface Si concentration. Using a Si flux, STM experiments have observed a sequence of transitions from $(\sqrt{3} \times \sqrt{3})$R30, $(2\sqrt{3} \times 6\sqrt{3})$R30, $(3 \times 3)$ and $(7 \times 7)$ structures as the surface Si concentration is increased [73, 77, 79]. LEED on the other hand has only observed the $(\sqrt{3} \times \sqrt{3})$R30 and $(3 \times 3)$ phases [56, 80] indicating that the $(2\sqrt{3} \times 6\sqrt{3})$R30 and $(7 \times 7)$ structures are due to local disorder. It is worth noting that an initial $(1 \times 1)$ LEED pattern has been seen by several groups immediately after introduction of the oxidized SiC(0001) surface into the vacuum [55, 81, 82]. The existence of the $(1 \times 1)$ pattern and its long range order seem to depend on how the original SiC surface was grown and treated. Regardless, this oxidized surface transforms to the familiar $(\sqrt{3} \times \sqrt{3})$R30 after heating above 1100 °C consistent with the $(\sqrt{3} \times \sqrt{3})$R30 being a Si depleted surface [55, 81, 83]. Whether or not a Si flux is used, heating above 1050 °C results in a well defined $(\sqrt{3} \times \sqrt{3})$R30 phase, further heating above 1100 °C causes a mixture of $(6\sqrt{3} \times 6\sqrt{3})$R30 and $(\sqrt{3} \times \sqrt{3})$R30 phases to develop. Continued heating above 1200 °C results in only the $(6\sqrt{3} \times 6\sqrt{3})$R30 pattern (diffraction spots unique to the $\sqrt{3}$ structure are extinguished.) (See figure 8.) This is the precursor structure before graphene forms.

Starke *et al* [84] have done a detailed comparison of the 4H-SiC $(\sqrt{3} \times \sqrt{3})$R30 surface prepared via three different techniques.

(1) Heating an *ex situ* prepared hydrogen-etched sample in UHV for 30 min at 950°.
(2) Preparing the silicon rich $(3 \times 3)$ in a Si flux phase and subsequently heating the sample for 30 min at 1000 °C.

[2] Cree Inc. 4600 Silicon Drive, Durham, NC 27703.

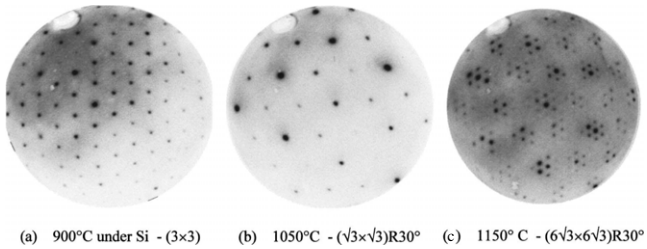


**Figure 8.** A sequence of LEED images following the temperature dependent surface reconstructions leading to the $(6\sqrt{3} \times 6\sqrt{3})$R30. Reproduced with permission from [56]. Copyright 1998 by the American Physical Society.

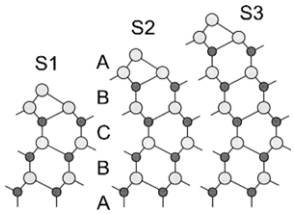


**Figure 9.** Different stacking terminations denoted as S1, S2 or S3 according to the number of identically oriented bilayers at the surface. Note that the S3 termination breaks the 4H bulk-stacking sequence. Large and bright spheres represent Si atoms, while small and dark spheres represent C atoms. Reproduced with permission from [83]. Copyright 2000 Elsevier.

**Table 3.** Relative concentrations of different surface stacking faults for different preparations of the $(\sqrt{3} \times \sqrt{3})$R30 structure. From [84].

| | Surface stacking (%) | | |
|---|---|---|---|
| Preparation method | S2 | S1 | S3 |
| (1) Annealing *ex situ* | 75 | 15 | 10 |
| (2) Direct preparation in Si flux | 50 | 15 | 35 |
| (3) Annealing the (3 × 3) phase | 20 | 15 | 65 |

(3) Heating the sample between 1000–1100 °C in a Si flux to avoid silicon depletion of the surface.

These different precleaning procedures ultimately lead to the $(\sqrt{3} \times \sqrt{3})$R30 structure, but with different SiC stacking faults just below the surface [83, 84]. The different types of faulted surfaces are shown in figure 9. Their relative surface fractions are given for different cleaning procedures in table 3. Starke *et al* [84] assert that the different stacking terminations are seeds for either cubic (S3 termination) or hexagonal growth that in turn can influence the degree of surface order. This statement might suggest that starting from a (3 × 3) versus a $(\sqrt{3} \times \sqrt{3})$R30 structure, or $H_2$ etching the substrate versus no pre-etching, might influence the graphene that is subsequently grown from these different starting surfaces. To date, no clear link has been made between these early preparation stages and the subsequent quality of the graphene films grown from them.

*3.2.2. Si-face growth.* After the precleaning process described in section 3.2.1, the SiC is heated to higher temperatures until graphene forms. An understanding of the onset of graphene formation has evolved over the last two decades. In the earliest studies, conducted by Muehlhoff *et al* [60], x-ray photoemission spectroscopy (XPS), Auger electron spectroscopy (AES) and electron energy-loss spectroscopy (EELS) data for both polar faces of 6H-and 15R-SiC polytypes revealed that the Si/C surface concentration on the (0001) Si-face was very stable up until ∼1030 °C. Above this temperature a 'massive surface segregation of C to the surface' occurs. They report features in EELS and XPS data characteristic of graphite at temperatures as low as 900 °C and that prolonged annealing at 1170 °C increases the graphitic carbon concentration. Recent work has revealed a more detailed series of steps leading to the formation of epitaxial graphene. These will be discussed in section 4.1.1. In this section we are concerned with a more global view of how graphene is grown and will focus on parameters that determine growth, film thickness and film quality.

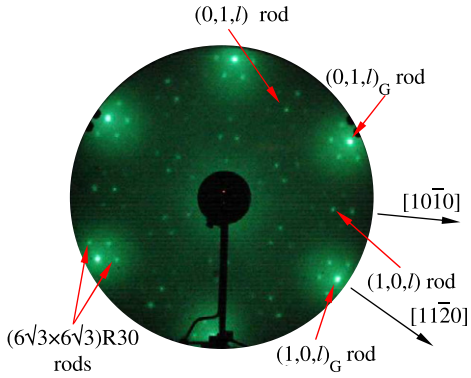


**Figure 10.** LEED image at 69.1 eV of a 4H Si-face graphene film (1–2 layers thick) showing the $(6\sqrt{3} \times 6\sqrt{3})$R30 reconstruction. The principal graphene $(1, 0, \ell)_G$ rod is aligned along the SiC [11$\bar{2}$0] direction. Also shown are the SiC rods: $(1, 0, \ell)$ and $(0, 1, \ell)$. The SiC [10$\bar{1}$0] direction is shown for reference.

While growth in other environments is just beginning to be investigated, to date all reported Si-face graphene is grown in a UHV environment. Because of difference in thermometry used by various research groups, it is difficult to compare their reported graphitization temperatures with a high degree of accuracy. Even though graphitic bonds begin forming as low as 1000 °C [78, 85], it is generally agreed that a carbon layer with a graphene structure only forms at temperatures above 1250–1350 °C [55, 56, 82]. Graphene grown on the Si-face surface of SiC grows epitaxially, rotated 30° from the SiC substrate commensurate with the pre-graphitized SiC(0001) $(6\sqrt{3} \times 6\sqrt{3})$R30 reconstruction (see figure 6) [54, 56]. A LEED pattern from a 1–2 layer graphene film is shown in figure 10. The LEED shows a 6-fold pattern from the graphene overlayer, faint integer order SiC rods that are attenuated by the graphene film and a large number of spots (rods) from the $(6\sqrt{3} \times 6\sqrt{3})$R30 reconstruction. Other structures besides the $(6\sqrt{3} \times 6\sqrt{3})$R30 have also been observed in small concentrations such as the (5 × 5) [55, 86]. Riedl *et al* [86] have shown that the amount of (5 × 5) present on the surface depends on which of three different preparation techniques described in section 3.2.1 is used to prepare the substrate. Figure 11(a) shows an STM image of the graphitized surface. The hexagonal graphene lattice is clearly apparent.

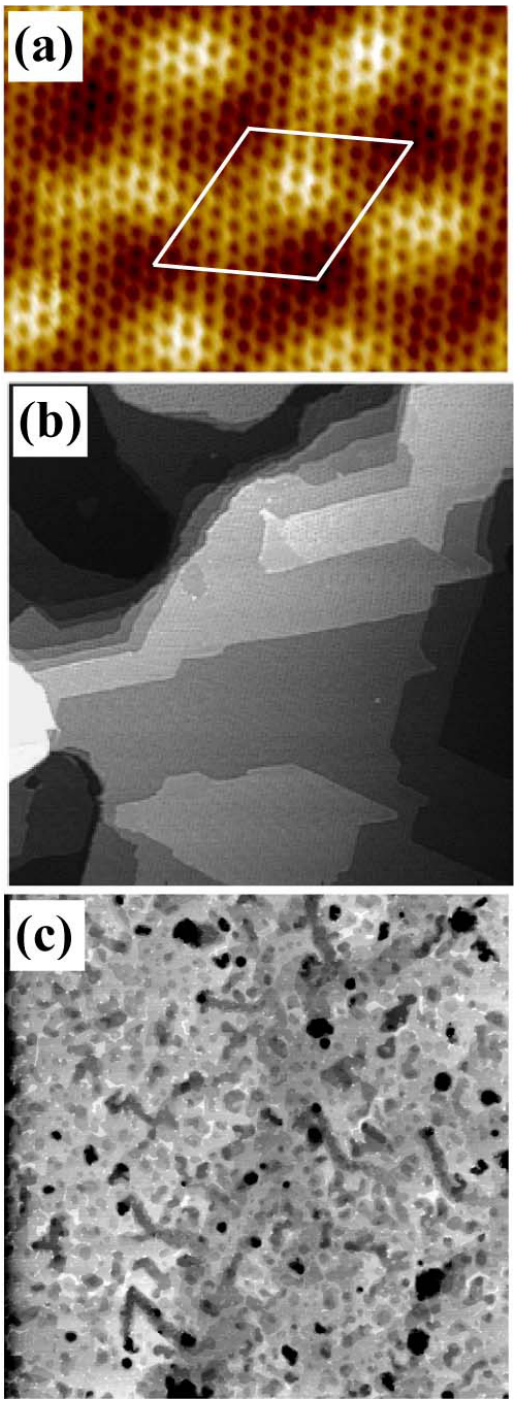


**Figure 11.** A series of STM and AFM images of UHV grown Si-face graphene. (a) (33 Å × 24 Å) STM image of a single graphene layer showing the hexagonal structure (tip bias was 0.75 V at 0.1 nA). The (6 × 6) unit cell is also shown for reference[3] . (b) Larger scale (1500 Å × 1500 Å) STM image taken with a bias voltage of −2 V (occupied states at 100 pA). Terraces are due to the roughness of the SiC substrate. The height difference between terraces correspond to a 6H-SiC half-cell step height (3 SiC bilayers) From [66]. (c) A larger AFM image (9 $\mu$m × 9 $\mu$m) of a 4H Si-face graphene film with 1–2 graphene layers. Image shows large scale roughness of the surface.

While LEED shows a $(6\sqrt{3} \times 6\sqrt{3})$R30 periodicity, STM images from many groups find a (6 × 6) unit cell (see figure 11(a)) [23, 55, 59, 64, 86–88]. The relationship between the STM measured (6 × 6) and the $(6\sqrt{3} \times 6\sqrt{3})$R30 structure measured by LEED has been the subject of much debate. We will, therefore, reserve a more thorough discussion of them until section 4.1.1 when we look at the details of the graphene/SiC interface structure.

The major problem with UHV grown Si-face epitaxial graphene production has been SiC substrate roughening as the graphene forms. This is demonstrated clearly in the STM and atomic force microscopy (AFM) images in figures 11(b) and (c). Even though the starting SiC substrate is composed of uniformly spaced SiC steps, the surface after graphitization is very rough with random steps and deep pits. A review of the published literature shows that the average SiC terrace size after graphitization is no larger than 500 Å and more typically 200 Å [14, 86, 89, 90] with an rms roughness of 0.17 Å [91]. This should be compared to 1–2 $\mu$m SiC terraces before graphitization. The substrate order (or lack of it) has turned out to be insensitive to surface pretreatment. Using a $H_2$ pre-etch, a Si flux to remove the surface oxide or preparing different starting surfaces as described by Riedl *et al* [86], all lead to similar terrace sizes as measured by AFM or STM [14, 86, 89, 90]. LEEM studies reach a similar conclusion [92]. It is worth noting that the majority step height in in the 6H-SiC graphitized surface in figure 11(b) is three SiC bilayers high [66]. This makes some sense because it is both the stacking fault period in the 6H polytype (see figure 5) and the approximate number of SiC bilayers needed to produce enough carbon for a graphene layer (see figure 7).

X-ray diffraction measurements by several groups put a lower limit on UHV grown graphene order to sheets that are typically ∼400 Å across regardless of whether or not the surface oxide was removed by Si deposition [27, 66]. The fact that the apparent graphene order measured by diffraction is similar to the substrate terrace length is not a coincidence since SiC steps make graphene sheets on adjacent terraces scatter incoherently. In fact the graphene order is significantly better than diffraction indicates despite the substrate roughness. This is because the graphene grows continuously over the step edges [89]. This is demonstrated in the STM image in figure 12 that shows a graphene sheet growing unperturbed over a 4H-SiC bilayer step (2.52 Å). Not only does the graphene grow over the SiC steps, but it has also been shown to grow over graphene steps [93]. It is clear from these studies that epitaxial graphene growth is very robust in spite of substrate roughness. The actual coherent size of a graphene sheet grown on SiC is difficult to estimate. The best estimates come from transport measurements that give values of the electron coherence length in Si-face graphene of ∼1000 Å [14].

Besides the inability to correlate pre-surface cleaning to graphene quality, attempts to associate increased graphene order by other means have also fallen short. Different heating techniques at graphitization temperatures have been used by various groups with the goal of producing more uniform graphene films. This includes both e-beam heating and resistive heating methods. E-beam heating has the disadvantage of producing large thermal gradients across the

[3] We thank M Hupalo and M Tringides for supplying these STM images.

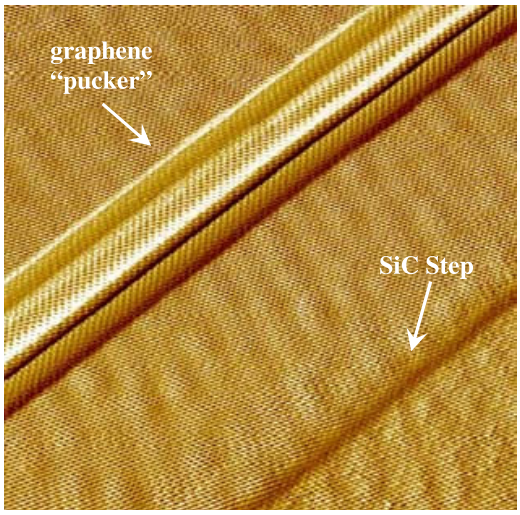


**Figure 12.** A derivative mode STM image (200 Å × 200 Å) of a one layer epitaxial graphene sheet grown on the 6H-SiC(0001) Si-face. The image was acquired at −0.2 V (empty states). The image shows the graphene growing over a substrate SiC bilayer step (∼2.52 Å). Also shown is a graphene 'pucker' described in the text. See footnote 3.

**Figure 13.** A 2.5 $\mu$m × 2.0 $\mu$m STM image of direct current heated 6H Si-face grown graphene film. The surface contains 85% single layer graphene with the remaining surface composed of 2 layer graphene. See footnote 3.

sample. It also heats the surrounding sample holder so that outgassing pressures during graphitization can reach $1 \times 10^{-8}$ Torr. Some groups have used cryogenically cooled sample mounts to keep the outgassing pressure to $<5 \times 10^{-10}$ Torr. To date, there are no comparative studies to gauge the effect of background pressure on graphene quality. However, STM experiments from groups with low and high outgassing pressures all report very similar graphene film order [24, 55, 94].

Recently the lack of progress in Si-face film growth has changed. Some very high quality graphene films have been produced from 6H-SiC in UHV by Hupalo *et al* [95]. Pressures during heating are kept below $5 \times 10^{-10}$ Torr by using resistive heating. Samples were not $H_2$ etched prior to graphitization and no Si flux was used to remove $O_2$. Their graphene is grown slowly through a series of short (∼30 s) heating steps at a graphitization temperature (between 1300 and 1350 °C as measured by an infrared pyrometer with $\epsilon = 0.9$). Using this method, the authors have been able to produce graphene films where the substrate roughness is essentially determined by the starting vicinality of the clean SiC wafer. Figure 13 shows a large scale STM images of a graphene film grown by this method. The image has a number of important features. First, unlike the highly faceted surfaces in figures 11(a) and (b) that are typical of current Si-face graphene films, the surface in figure 13 shows the well ordered step structure of the original clean SiC substrate. The second important feature of these graphene films is the graphene uniformity. The film in figure 13 is composed of 85% single sheet graphene (the remaining surface is two layer graphene). This is a significant improvement in the ability to control graphene film thickness. Early claims of layer-by-layer graphene growth [66] on Si-face SiC have never been substantiated with any structural evidence. In fact it is very clear from recent low energy electron microscopy (LEEM) [28, 92] and STM [66, 86] experiments that multilayer graphene islands are prevalent throughout the surface.

### *3.3. C-face graphene production*

*3.3.1. C-face pre-graphitization.* Compared to the Si-face, there have been fewer studies of the SiC C-face. As with the Si-face, SiC samples have been prepared with a number of different pre-treatment procedures. Samples that were only $H_2$ etched prior to introducing them into UHV have a SiO layer with a $(\sqrt{3} \times \sqrt{3})$R30 reconstruction [81, 96]. Heating this surface in UHV leads to a number of different reconstructions: heating to 1050 °C for 15 min removes the oxide and gives a $(3 \times 3)$ reconstruction [96, 97], continued heating to 1075 °C produces a $(2 \times 2)_C$ phase in coexistence with the $(3 \times 3)$ phase [98]. The subscript 'C' is used to distinguish this phase from a $(2 \times 2)_{Si}$ phase that is formed by depositing Si on a graphitized SiC surface at 1150 °C (see section 3.3.2) [98]. Seubert *et al* [99] have determined the surface stacking sequence for 6H C-face samples for well annealed surfaces with the $(2\times2)_C$ phase. While well annealed Si-face samples with a $(3 \times 3)$ phase break the hexagonal stacking, the C-face prefers to maintain the S1 hexagonal stacking shown in figure 9.

Other groups remove the initial surface oxide while preserving the substrate order by heating in UHV to ∼850°C in the presence of a Si flux [62, 78] or a Ga flux [73]. The initial $(1 \times 1)$ pattern transforms into a $(3 \times 3)$ reconstruction following these treatments [62, 97, 100–102]. When heated above ∼1050°C the $(3\times3)$ structure transforms to the $(2\times2)_C$ reconstruction [61, 62]. Figure 14 shows a sequence of LEED patterns from a 6H-SiC C-face sample heated to different temperatures in UHV with a Si flux. A number of groups have studied the effects of Si surface concentration on the pre-graphitized surface reconstructions. The $(3 \times 3)$ can be transformed into a $(\sqrt{3} \times \sqrt{3})$ by heating at 950°C in the presence of a Si flux [55, 59]. Reannealing to 850°C reversible transforms the surface back to $(3 \times 3)$ structure.

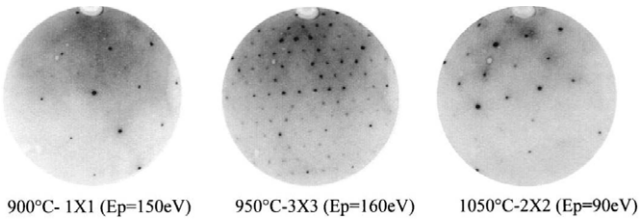


**Figure 14.** A sequence of LEED images for different temperatures during the pre-graphitization of the 6H-SiC C-face surface in the presence of a Si flux. $E_P$ is the incident electron energy. Reproduced with permission from [61]. Copyright 1999 Elsevier.

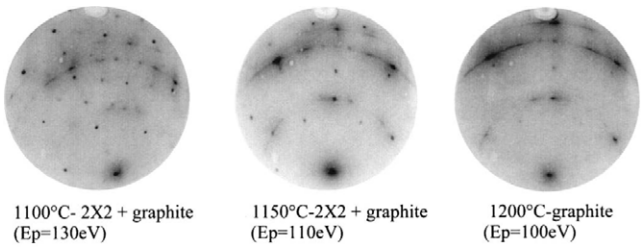


**Figure 15.** A sequence of LEED images for different temperatures during the graphitization of 6H-SiC C-face. $E_P$ is the incident electron energy. Reproduced with permission from [61]. Copyright 1999 Elsevier.

The structures of these different reconstructions are not completely understood. It is generally thought that the $(\sqrt{3} \times \sqrt{3})$ structure is due to Si adatoms absorbed on the $T_4$ sites of the carbon surface [55, 59, 103]. This explanation is consistent with XPS results that show surface carbon enrichment (i.e. the loss of Si atoms) begins at 600–1000 °C on the C-face [60]. The Si-adatom model also explains why a Si flux is necessary to maintain the $(\sqrt{3} \times \sqrt{3})$ structure when the surface is heated above 600 °C. The $(2 \times 2)_C$ structure is also thought to be made of Si adatoms [99]. Instead of the $T_4$ sites, the Si atoms lie in $H_3$ sites but with a lower density than the silicon in the $(\sqrt{3} \times \sqrt{3})$ structure.

*3.3.2. C-face graphene growth.* When heated above ∼1100 °C in UHV the $(2 \times 2)_C$ LEED pattern on the clean SiC C-face surface begins to transform to a mixture of $(2 \times 2)_C$ and graphene. By ∼1200°C the $(2 \times 2)_C$ disappears and the graphene diffraction pattern is fully developed [61, 62]. LEED images show that there is an azimuthal broadening indicating a good deal of rotational disorder in the graphene sheets (see figure 15). Like the Si-face, the hexagonal diffraction pattern from the graphene is principally rotated 30° relative to the SiC but no evidence of the $(6\sqrt{3} \times 6\sqrt{3})$R30 diffraction rods have been observed. Above ∼1200 °C the films are sufficiently thick that the electron beam is attenuated enough that no SiC diffraction rods are observed. Forbeaux *et al* [62] have measured *k*-resolved inverse photoemission spectroscopy, KRIPES, spectra during the graphitization process. They find that a graphene $\sigma^*$ state appears in the spectra as low as 1100°C indicating the start of graphitic bond formation. This is consistent with early XPS measurements [60].

There are very few published studies of either the morphology or the band structure of UHV grown C-face graphene. This is most likely due to the streaking in LEED images, that led early investigators to conclude that C-face films were of poor quality and rotationally disordered [54, 61, 62]. The disorder was also seen in early STM studies of UHV grown C-face films that found high concentrations of graphene nanocaps on the surface [81, 104]. These nanocaps are similar to those that have been identified as precursors to the formation of nanotubes on the SiC C-face in a high pressure furnace environment [105–107].

Only recently have exceptionally high quality graphene films been grown on the 4H-SiC C-face in a RF furnace [27]. The furnace is evacuated by a turbopump but details of the vacuum environment at the sample position are not known because the small furnace volume makes pressure measurements difficult. It is estimated from conductance that the pressure at the sample position is between $P \sim 10^{-4}$–$10^{-3}$ Torr. Temperatures are measured with a WRe thermocouple on the sample enclosure. The SiC samples are heated to 1200 °C for ∼20 min to outgas the furnace and remove surface oxides from the SiC. After this step the furnace is quickly ramped to the graphitization temperature. In this furnace environment the minimum graphitization temperature is 1420 °C. This temperature is significantly higher than the minimum graphitization temperature required to grow graphene in UHV on C-face SiC. The graphene film thickness can be controlled by both the growth temperature and growth time (see section 3.4). At 1420 °C a 4–5 layer graphene film forms in ∼6 min [108]. This relatively fast growth rate means it is difficult to produce very thin graphene layers because the furnace's thermal mass prevents rapid temperature control. Thickness measurements using AES prove to be unreliable for furnace grown graphene for a number of reasons. Firstly, the graphene film thickness is usually much larger than the Auger electron penetration depth and secondly, residual Si is known to accumulate at the graphene/vacuum interface. Therefore ellipsometry or x-ray diffraction [27, 108] have been used to estimate film thicknesses for these C-face graphene films (see section 4.3).

The quality of the graphene grown by this method is exceptionally good. Initial x-ray studies of furnace grown 4H-SiC C-face graphene films measured a lower limit on the average coherent size of the graphene to be 3000 Å and a surface rms roughness of <0.05 Å [21]. However, like the Si-face, STM images show that the C-face graphene also grows over the SiC steps limiting diffraction coherence lengths [109]. Better estimates of the graphene quality come from AFM and STM measurements. Figure 16(a) shows an AFM image from a furnace grown 10–15 layer graphene film on the 4H-SiC C-face. Unlike most UHV grown Si-face films, the furnace growth method for C-face films nearly preserves the pre-graphitized substrate step density (typical SiC terrace widths are (>1 $\mu$m). The bright lines running through the AFM image in figure 16(a) are not cracks or grain boundaries in the graphene film. They are graphene 'puckers' due to the thermal expansion difference between graphene and SiC as the samples are rapidly cooled after graphitization. These 'puckers' are similar to those seen in figure 12 on high quality Si-face graphene films and have

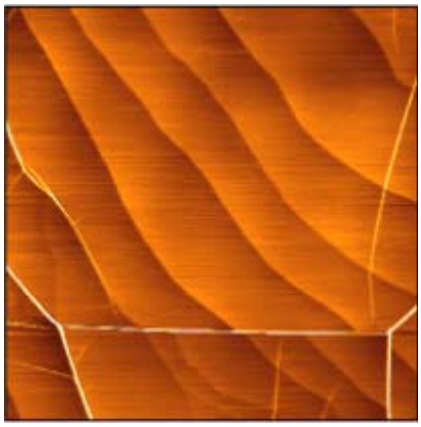

**Figure 16.** A 8$\mu$m × 8 $\mu$m AFM image of a 10–12 layer graphene film grown on the SiC(000$\bar{1}$) C-face in a furnace environment [108]. Lines are 'puckers' in the graphene similar to those shown in figure 12.

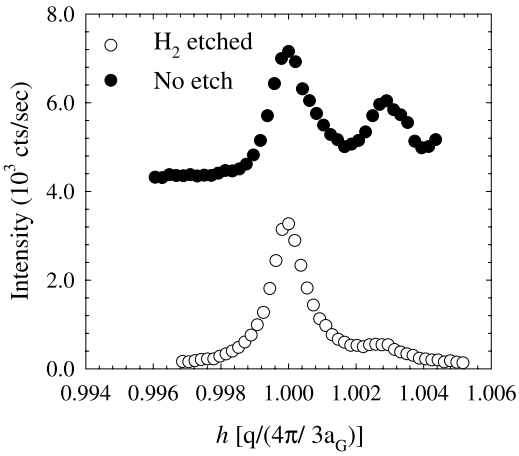


**Figure 17.** Radial $h$ scans through the graphene $(h = 1, 0, \ell)_G$ rod ($q_z = 2\pi\ell/c_G$ for $\ell = 0.033$) for $H_2$ etched and unetched graphene films grown on the C-face of SiC. The background in the $H_2$ etched sample is suppressed by a factor of 150 over the unetched substrate.

also been observed in graphene grown on Ni surfaces [58]. The fact that these 'puckers' run continuously over many SiC steps indicates that the graphene films are likely to be continuous over very large distances (>9 $\mu$m). Point defect densities (i.e. missing atoms or impurities) in these films are difficult to estimate. Raman spectroscopy offers sensitivity to these defects through a higher order scattering process over a beam size of 10–100 $\mu$m [110, 111]. In particular the D-band near 1350 cm$^{-1}$ is known to be sensitive to impurities and defects in the lattice. Raman experiments on furnace grown C-face epitaxial graphene conclude that the D-band is absent [121] indicating that the defect concentration in these films is very low.

While most of the SiC C-face surface preparation techniques described in section 3.3.1 have little or no effect on the quality of the graphene films grown on the C-face, the $H_2$ pre-etching process does. Even though a comparison of $H_2$ etched and unetched graphitized samples by AFM show no discernible difference in the sample quality, x-ray diffraction detects both a high degree of point-like defects and surface faceting at the surface [112]. Figure 17 shows radial scans ($h$ scans) through the $(h = 1, 0, \ell)_G$ graphite rod (see figure 10) at grazing incidence for graphene grown on the C-face of SiC for both a $H_2$ etched and unetched surface. The main peak at $h = 1.0$ is the graphene $(1, 0, \ell)_G$ rod and the secondary peak at $h = 1.0024$ is due to strained graphene from rotational faults in the multilayer film that will be discussed in section 4.2. The main difference between the two scans is a 150-fold increase in the diffuse background of the unetched sample. This points to a high density of point defects or another type of local disorder at the interface. Highly tilted surface rods are also observed in unetched films [112] and indicate that the unetched samples have a high density of SiC surface facets. While the graphene film is most likely not affected by this disorder, dangling SiC bonds associated with these defects should influence the charge transfer between the SiC interface and the first few graphene layers [20].

A final note about the quality of these films can be inferred from the transport properties of devices made from furnace grown C-face films. Kedzierski *et al* [29] have been able to fabricate hundreds of epitaxial graphene gates over many square millimeters on a single SiC chip with mobilities up to 5000 cm$^2$ V$^{-1}$ s$^{-1}$ and on/off current ratios of up to 7. What is most exciting is that graphene devices fabricated over such a large length scale have a functional yield of up to 95% with a very small distribution of mobilities from switch to switch. This result demonstrates the long range order that is achievable in furnace grown epitaxial graphene on SiC.

### *3.4. Growth kinetics*

While it is clear that the C-face films grown in an RF furnace are of very high quality, little is known about the growth kinetics on either polar face of hexagonal SiC. Ong and Tok [113] have done an STM study of the development of the $(6\sqrt{3} \times 6\sqrt{3})$R30 phase that precedes graphitization on the Si-face of SiC. Starting from the Si-rich (3 × 3) phase, they follow a sequence of steps involving the formation different Si clusters that leads to a carbon rich surface. However, outside this study, kinetics information about the growth of graphene must be gleaned from a number of unrelated experiments. In this section we will review what is and is not known about graphene growth on SiC.

The growth of graphene appears to be essentially independent of whether or not it is grown from 4H- or 6H-SiC substrates. This is demonstrated in figure 18 where the number of graphene layers as a function of growth temperature is plotted for both 4H- and 6H-SiC substrates. This result is a bit surprising since the half-cell stacking fault in the 6H polytype is 3-bilayers compared to 2-bilayers in the 4H polytype. Because the carbon in ∼3-bilayers is needed to produce a single graphene layer, it would seem that 6H-SiC would be more conducive to a layer-by-layer growth mode. There is some evidence based on AES that graphitization on 4H-SiC appears to start 50 °C higher compared to 6H-SiC, but relative error bars on both absolute temperature and the graphene thickness measurements make these claims hard to

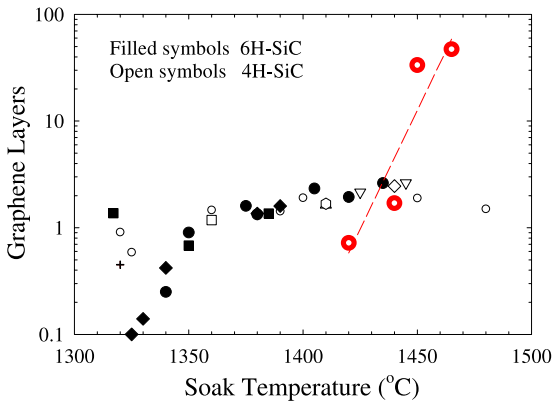


**Figure 18.** The number of graphene monolayers grown in UHV on Si-face SiC for different soak temperatures as determined by AES (see section 4.3 for details of AES estimate). Temperature was measured with an optical pyrometer. Filled symbols are for 6H-SiC substrates and open symbols are for 4H-SiC substrates. Symbols represent different soak times: (+) 3 min, (◇) 5 min, (○) 6 min, (▽) 7 min, (△) 8 min and (hexagon) 20 min. Partially filled circles are for furnace grown graphene on the C-face of 4H-SiC (thickness determined by ellipsometry). Dashed line is a guide to the eye. From [112].

prove [63, 64]. There are, however, fundamental differences in the kinetics between graphene grown on the Si-face and C-face and whether or not they are grown in UHV or in a furnace environment. XPS, AES and EELS all indicate that on the Si-face the UHV grown graphene film thickness increases slowly while on the C-face the films grow much faster [60].

The minimum temperature for the formation of graphitic bonds, as determined by KRIPES spectra, is approximately the same for UHV grown Si-face and C-face graphene (∼1080–1100 °C measured by an infrared pyrometer using an assumed emissivity of 0.9) [62]. The data in figure 18 shows the onset of graphitization occurring at a much higher temperature, ∼1350 °C. Another interesting feature of UHV Si-face grown graphene is that the number of layers grown is relatively insensitive to the growth time and seems to only depend on the growth temperature (see figure 18). In contrast, furnace grown C-face graphene depends on both temperature and growth time [108]. Also note in figure 18 that the thickness of furnace grown C-face graphene is a rapid function of temperature.

We can conclude that kinetics at the graphene/SiC interface control the growth of graphene. This follows for a number of reasons. First, there is no significant bulk diffusion at the graphitization temperatures [69, 70]. Second, diffusion through the graphene film and sublimation of atoms or molecules containing Si or C from the graphene/vacuum interface must be the same for graphene grown on both surfaces. Finally, there are real structural differences in the interface between SiC and graphene on the Si-face and the C-face (see section 4.1) that potentially affect activation barriers for diffusion of either C or Si. The conclusion that the graphene/SiC interface controls the graphene growth kinetics is independent of whether or not each new graphene layer grows at the graphene/SiC interface or at the graphene/vacuum interface. While there have been no published experimental investigations of the growth kinetics of epitaxial graphene, there is indirect evidence that suggest a number of kinetic processes that may be key to understanding and controlling the production of epitaxial graphene.

Graphene growth on both polar faces requires diffusion of Si to the vacuum interface where it can be removed. An estimate of Si diffusion through graphite shows that Si can readily diffuse through the growing graphene film at the graphitization temperature [114]. Regardless of the exact mechanism to remove Si from the vacuum/graphene interface, the rate of diffusion of Si, or some Si complex, through the graphene film must be the same on either polar face. These observations point to a Si diffusion limitation at the graphene/substrate interface. To explain the differences in graphene growth on the two polar faces, the removal of Si from the interface must be different for the Si-face and the C-face. This is consistent with evidence from XPS that carbon enrichment at the surface occurs between 600 and 1000 °C on the C-face, while no significant carbon enrichment is observed on the Si-face in the same temperature range [60]. The slower rate of Si removal from the interface on the Si-face of SiC would also explain the higher surface roughness after graphitization. It is known from studies of SiC growth that on the Si-face excess Si nucleates on the SiC terraces and gives rise to faceting and twinning [115]. Si that is trapped at the graphene/SiC interface would recrystallize as SiC clusters on the SiC terraces that would then nucleate islands that ultimately cause the surface to roughen.

Another important factor in graphene growth is the environment. In section 3.3.2 it was shown that furnace grown graphene on the C-face grows in very large films with little roughness in the SiC surface. Also, while UHV grown C-face graphene begins to grow ∼100–150 °C lower than Si-face graphene [56, 61], the growth temperature of furnace grown C-face graphene is shifted to higher temperatures. This is demonstrated in figure 18. The differences between the growth of graphene in UHV and a furnace environment are not understood. In part this is due to the lack of any detailed knowledge of the furnace atmosphere. Regardless, there is evidence that enhanced Si diffusion occurs in an $O_2$ atmosphere. It has been suspected for some time from experiments on the growth of CNTs on the C-face of SiC that active oxidation of Si occurs through diffusion of oxygen to the substrate [105–107]. SiO gas is transported back to the graphene/vacuum interface where it desorbs. Kusunoki *et al* [105], using a transmission electron microscope (TEM) equipped with energy-loss optics, were able to measure the oxygen K-edge loss feature across the CNT/SiC boundary from thin cross-sectioned samples grown in a furnace environment at 1300 °C. The measurements clearly show an oxide buildup at the CNT/SiC interface. It has also been noticed that the production of ozone near the SiC surface, by exposure to x-rays in air, produces SiO at the surface of thick graphene films [112]. This process occurs at room temperature suggesting that ozone rapidly leaches Si from the graphene/SiC interface to the surface.

It has been conjectured that the oxidation of Si at the interface occurs through three possible reaction paths

[105, 107]:

$$\mathrm{SiC} + \tfrac{1}{2}\mathrm{O_2(gas)} \rightarrow \mathrm{C(s)} + \mathrm{SiO(gas)} \quad (4a)$$

$$\mathrm{SiC} + \mathrm{CO(gas)} \rightarrow 2\mathrm{C(s)} + \mathrm{SiO(gas)} \quad (4b)$$

$$\mathrm{SiC} + \mathrm{H_2O(gas)} \rightarrow \mathrm{C(s)} + \mathrm{SiO(gas)} + \mathrm{H_2(gas)}. \quad (4c)$$

In all three reactions $O_2$ gas diffuses to the interface and reacts with the SiC to form SiO gas, which can diffuse out of the interface and through the graphene where it can desorb from the surface. These processes are estimated to proceed in the pressure range of $10^{-2}$–$10^{-6}$ Torr at temperatures between 1200–1600 °C [106].

SiO gas is also suspected to drive the formation of CNTs on the C-face of SiC by causing the formation of nanocaps either on the SiC terraces or at step edges. The caps form when the partial pressures of SiO at the SiC substrate boundary exceed the vacuum partial pressures. This leads to a net force that lifts the graphene from the surface and causes caps or nanotubes to grow [116]. The effect of these oxidation processes is expected to be very different for a UHV and furnace environment. In UHV the partial pressure of these gases is much lower than in the furnace atmosphere and may enhance nanocap formation.

Another consideration is that the vapor pressure of Si in furnace environments can be relatively high. In a furnace, Si may be in near equilibrium with the sample and the furnace walls through either SiO gas or a direct flux of Si atoms that are continually deposited on to, and subsequently evaporated from the hot oven walls. There are a number of possible roles that a Si flux can play on the growing film. Bernhardt *et al* [98] have shown that depositing Si in UHV on a graphitized C-face at 1150 °C causes the $(1\times1)$ graphene pattern to transform into a Si-rich $(2\times2)_{Si}$ phase. Continued heating of this phase at 1050 °C causes the surface to revert back to the pre-graphitized $(3\times3)$ phase. This suggests that Si can etch the graphene film. In a furnace environment a high $O_2$ pressure can oxidize Si deposited on the graphene surface and desorb as SiO gas. This process would prevent substantial diffusion of $O_2$ to the SiC–graphene interface, thus lowering the partial pressure of SiO at this boundary. Clearly a good deal of work remains before a complete understanding of the the growth of graphene on SiC is possible.

### *3.5. Exfoliated graphene*

Mechanically exfoliated graphene has been used as a prototype for studying the properties of an idealized single isolated graphene sheet. While exfoliated graphene is not scalable to device applications, it is still worth discussing what is structurally known about these systems as a comparison to epitaxial graphene. In particular it must be realized that exfoliated graphene is far from an idealized isolated system due to processing and the disorder and interactions introduced by laminating them to either a substrate or a support. Even 'unsupported' exfoliated graphene [117] starts with a graphene sheet deposited on a substrate that is subsequently chemically etched away. This process will leave a 'memory' of the initial substrate's structure on the sheet's topography. Despite claims to the contrary, a direct comparison between the structural order parameters of exfoliated graphene and epitaxial graphene show that exfoliated graphene is in general more disordered.

The process for producing single graphene sheets involves mechanically exfoliating single crystal graphite followed by placing them on a $SiO_2$ substrate [13]. The flakes are exfoliated by mechanical rubbing or are peeled off with Scotch tape [6, 13]. Some work has been done on chemically exfoliating graphene from graphite, but since most transport measurements have been done on mechanically exfoliated flakes [118], we will restrict our discussion to the mechanically produced flakes.

TEM experiments on unsupported exfoliated graphene have shown that the graphene sheet has a ±5° variation in the surface normal [117]. This huge surface mosaic is nearly two orders of magnitude larger than even the poorest SiC grown graphene (a lower bound of 0.06° can be estimated from the graphene rod width in [27]). The huge mosaic angle corresponds to surface height fluctuations of 10 Å. As a comparison, the rms surface fluctuation on C-face grown graphene is <0.05 Å [21]). It has been suggested that the mosaic is due to a 2D Mermin–Wagner instability [119] in the film [117]. This claim has never been tested and is unlikely ever to be confirmed given the large amplitude oscillations measured. It is much more likely that the mosaic is due to defects in the graphene caused by either the exfoliation process, the initial substrate roughness or the wet chemistry involved in forming the unsupported film. Because there are no studies of the chemical contamination in exfoliated films, it is not possible to comment on the role of impurities on the graphene roughness. It is clear however, that the roughness of exfoliated graphene is more endemic and not the sole property of unsupported graphene. The main support for this conclusion is that the rms roughness in exfoliated graphene supported on $SiO_2$ surfaces is nearly the same as unsupported graphene. Stolyarova *et al* [120] have used both STM and AFM to measured peak-to-peak height fluctuations of 8–15 Å over a 200 × 200 Å area. This should be contrasted to the measured roughness on C-face films that are less than 0.05 Å over a 3000 × 3000 Å area [21]. It seems that exfoliated graphene is more like crumpled paper than the 2D films grown epitaxially on SiC.

Another important structural property is the point defect density in graphene. Raman experiments have shown that D-band peak is absent in both exfoliated [111] and C-face epitaxial graphene [121]. Since the D-band is known to be sensitive to impurities and defects in the lattice, it can be concluded that the defect concentration is comparably low in both materials.

## 4. The structure of epitaxial graphene on SiC

To bring some coherence to subsequent discussions of both Si-face and C-face epitaxial graphene and their respective interface with SiC, we will define a standard model for the graphene/SiC interface. As will be shown, the model is the result of a rough consensus of many experiments. This will be particularly helpful in bringing some unification to the labeling

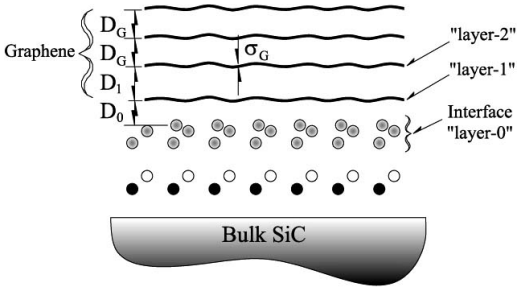


**Figure 19.** A schematic model of the graphene/SiC interface. The model consists of the bulk with a last layer that may be reconstructed and an interface layer ('layer-0') between the bulk and the graphene film. $\sigma_G$ is the rms height variation in the graphene layer. $D_0$ is the distance from the last atom in the interface layer and the first graphene layer.

of graphene layers that has been confusing in the literature. It will also be helpful in in section 4.3 where we discuss how the number of graphene layers grown on SiC are estimated. The interface model is shown in figure 19. It consists of bulk SiC where the last bulk SiC bilayer may or may not be relaxed. Between the bulk SiC and the graphene film is a reconstructed interface layer that we will refer to as 'layer-0'. The first graphene 'layer-1' is a distance $D_0$ above the topmost atom in the interface layer. $D_1$ is the spacing between the first and second graphene layers and $D_G$ is the spacing between subsequent layers (note that $D_G$ is not necessarily equal to the bulk graphite spacing $c_G/2$). We have also defined an rms height variation $\sigma_G$ of a graphene layer. $\sigma_G$ includes both height variations due to a reconstruction in the graphene and any roughness in the graphene film. The SiC substrate roughness (e.g. due to steps, etc) $\sigma_{SiC}$ is not shown in the figure.

We begin the comparison of graphene structure on the two polar faces of SiC with the SiC(0001) Si-face. The structure of graphene and the graphene/SiC interface, along with its electronic band structure, have been more extensively studied on this face. While SiC(000$\bar{1}$) C-face films have been the focus of transport measurements on epitaxial graphene, this surface has only recently been the subject of many new structural studies. These recent investigations show some remarkable structural characteristics of C-face films that begin to explain their transport properties. One word of caution should be given at this point when viewing graphene STM images in the following sections. In principle the STM micrograph of an isolated graphene sheet should image all six atoms in the graphene ring. STM data from epitaxial graphene often images every other atom and may lead to the assumption that the broken symmetry in the image is due to AB . . . stacking. This is not necessarily correct. STM imaging of carbon atoms in the graphene ring is much more complicated and depends on a number of factors including sample-tip bias. For analysis of these effects the reader is referred to [93, 122] and [123].

### *4.1. Graphene–SiC interface*

*4.1.1. Si-face structure.* In order to understand the electronic properties of Si-face graphene films it is critically important to know the graphene/SiC interface structure. The discussions in sections 3.2.1 and 3.2.2 showed that the $(6\sqrt{3} \times 6\sqrt{3})$R30 periodicity immediately preceding the formation of a graphene persists after the graphene has formed on the Si-face of SiC (for brevity we will refer to this reconstruction as the $6\sqrt{3}$ structure). Despite many early studies of the pre-and post-graphitized Si-face $6\sqrt{3}$ termination, very little has been agreed upon about its structure. Early work questioned if the post-graphitized $6\sqrt{3}$ structure was indeed real. However, it is now clear that the pre-graphitized $6\sqrt{3}$ periodicity remains intact at the buried interface between the SiC bulk and the growing graphene film. This conclusion has been the result of many experiments that probe the interface between the SiC and the graphene once the graphene layers have formed. In this section we will review the results of experiments on the buried graphene/SiC interface and sift through the many, and sometimes contradictory, results to arrive at a model for the structure of graphene grown on the Si-face of SiC.

Early studies of the graphitization of the Si-face presumed that the $(6\sqrt{3} \times 6\sqrt{3})$R30 pattern was due to the commensurate alignment of a graphene overlayer with the SiC surface (figure 6(a)), forming a moiré pattern [54, 59, 87]. Early SXRD studies supported the moiré pattern idea because they failed to observe the $6\sqrt{3}$ rods [66]. The inability to observe these rods is not surprising due to the weak x-ray scattering cross section and the degree of disorder in the SiC surface. Early STM experiments also supported the LEED multiple scattering claim because they imaged a $6 \times 6$ reconstruction [55, 59, 64, 87, 88] instead of the $6\sqrt{3}$ pattern observed in LEED. However, more recent detailed STM studies have shown that the $6\sqrt{3}$ structure is topographically real [25, 86]. The ability to image the $6\sqrt{3}$ structure depends on the tunneling conditions. The $6 \times 6$ reconstruction is more pronounced at high tunneling bias (where most early studies where performed) while the $6\sqrt{3}$ is imaged at low bias (<1 V) [25, 86]. More evidence that the $(6\sqrt{3} \times 6\sqrt{3})$R30 structure is indeed real, has been given by Riedl *et al* [86]. They show that the amplitude of the $6\sqrt{3}$ modulation in the STM images decreases as the graphene layer thickness increases. This demonstrates that a substrate induced modulation from a real $6\sqrt{3}$ period is forced on the graphene film.

Part of the confusion over when graphene actually forms arose from over-interpreting LEED images. Because of the near commensurate graphene and SiC lattices, the integer order graphene LEED spots $((1, 0, \ell)_G$, $(0, 1, \ell)_G$, etc) in figure 10 are coincident with diffraction spots from the SiC $(6\sqrt{3} \times 6\sqrt{3})$R30 pattern (e.g., $(\frac{13}{6\sqrt{3}}, \frac{13}{6\sqrt{3}}, \ell)$). It is thus difficult to distinguish from LEED images alone when the $6\sqrt{3}$ spots transform from being a result of diffraction from a substrate structure to being caused by diffraction from a graphene layer. The LEED analysis is further complicated because the diffraction is an average over a ∼0.5 mm beam diameter. STM and LEEM data clearly show that over these areas different parts of the surface are in different stages of graphitization [28, 86, 92]. Nonetheless, more recent detailed LEED studies, correlated with STM results, show that the $(6\sqrt{3} \times 6\sqrt{3})$R30 structure is a precursor

phase to graphene formation. This structure remains at the SiC/graphene interface, although slightly altered, after graphene has formed [86]. This is the consensus from recent works by many groups that an intermediate surface structure with a $(6\sqrt{3} \times 6\sqrt{3})$R30 periodicity appears after the $(\sqrt{3} \times \sqrt{3})$R30 pattern disappears, but before a graphene layer forms [25, 82, 86]. The intermediate phase points to a reconstructed layer that remains at the boundary between the bulk SiC and the growing graphene. We will refer to this reconstructed layer as the 'interfacial layer 0' shown schematically in figure 19.

STM, using multiple biasing techniques, has been able to image through a graphene layer to study the interface layer structure [25, 94]. Figure 20 shows a series of STM images from three different parts of a sample that show atomic steps between terraces with different structures and electronic properties. They are labeled as layer-0 layer-1 and layer-2. STM and scanning tunneling spectroscopy (STS) measurements show that layer 0 has a 400 mV band gap (at 4 K) and is separated by a 2.5 Å up step from layer-1. An STM comparison of the uncovered layer-0 and the buried layer-0, seen by imaging through layer-1, show that the two structures are very similar and have identical periodicity.

A number of STM studies have confirmed the difference between the $6\sqrt{3}$ surface and the graphitized SiC surface. These studies have proposed models for the interface layer that consists of hexagons and tetramers like those shown in figure 20(e) [23, 55, 86, 88, 94, 113]. While there are similarities between these interface models, the structure and composition of this layer is not fully known. For instance, in the model of Rutter *et al* [25] the interface layer was chosen to be all Si because features of the reconstruction appear similar to features in the Si(111) (7 × 7) reconstruction. Chen *et al* [88] image a hexagonal structure similar to that shown in figure 20(e) and label it a 'carbon nanomesh' because they claimed it to be composed of carbon only. This claim is based on their XPS studies. However, this result is at odds with many other spectroscopic studies and may be due to the fact that they only analyzed the C(1s) peak without collecting similar data on the Si(2p) spectra. A more complete XPS study by Johansson *et al* [82] also concludes that there is a large amount of non-graphitic carbon involved in the $6\sqrt{3}$ surface but they go on to show that Si is also present in the surface layer. Three different C(1s) XPS peaks: the bulk SiC carbon peak, a graphitic carbon peak and a third unassigned (non-graphitic) carbon peak point to carbon tied up in bonds in an interfacial region. Furthermore the strength of surface component spectra implies more than one layer is affected by the $6\sqrt{3}$ reconstruction, as opposed to the $(\sqrt{3} \times \sqrt{3})$ reconstruction that appears to come from a single layer. Ong and Tok [113] have combined XPS and STM to study the $6\sqrt{3}$ surface up to temperature below graphitization (1100 °C). They argue from their XPS data that the surface consists of a SiC bilayer partially depleted of Si, with Si adatoms bonded to remaining parts of the Si in the first SiC bilayer. This leads to a structure that is ∼40% silicon atoms. They interestingly point out that Grass *et al* [124] have shown that four Si atoms form stable clusters on HOPG. In between the Si clusters in their model are regions

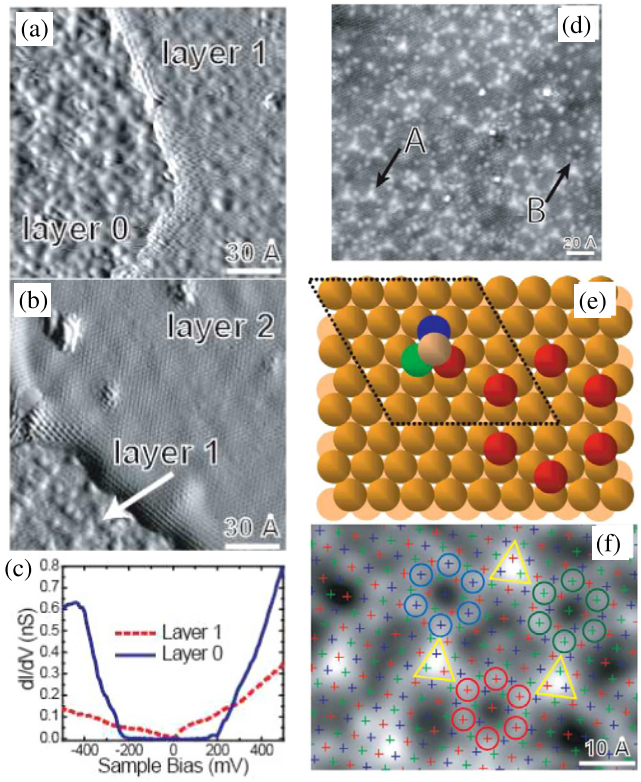


**Figure 20.** (a) STM image showing two regions (layer 0 and layer 1) separated by a 2.5 Å step ($V_t = 600$ mV and $I_t = 100$ pA). (b) STM image showing a 3 Å step up from the first graphene layer to the second layer ($V_t = 300$ mV and $I_t = 100$ pA). The image gray scale is proportional to the horizontal gradient of the topographic height for visual clarity of the two terraces for both images. (c) Differential conductance measurements obtained on the layer 1 and layer 0. (d) STM image of the first graphene layer (layer 1) showing a combination of SiC interface features (layer 0) along with the graphene lattice (layer 1) due to the transparency of the graphene ($V_t = 400$ mV and $I_t = 50$ pA). Typical adatom features are tetramers (labeled A) and hexagons (labeled B). (e) Schematic geometry of possible Si-adatom features consisting of one tetramer and hexagon. The three different colors (red, blue and green) correspond to Si adatoms on three different sublattices as in (f). (f) Magnified image of layer 0 (imaged through a graphene layer). Three hexagons are observed to lie on the three different SiC $\sqrt{3} \times \sqrt{3}$ sublattices, denoted by the three different colors. Tetramer features (yellow triangles) are what allow hexagons to switch to different $\sqrt{3} \times \sqrt{3}$ sublattices. Reproduced with permission from [25]. Copyright 2007 by the American Physical Society.

of exposed C atoms. While they note the possibility of C–C bonds forming within these regions to tie up carbon dangling bonds, it seems energetically difficult to reconcile such a large fraction of broken carbon bonds. Because they did not report the effects of multiple bias imaging, it may be that there are more atoms than their images infer.

Surface x-ray diffraction, SXRD, studies of the graphene–SiC Si-face system have also been used to determine the structure of the graphene/SiC interface [91]. X-ray reflectivity experiments measure the density gradient perpendicular to the surface. The data suggest two similar model structures for the interface region between the bulk and the graphene: the 'C-adatom' and 'Si-adatom' models shown in figure 21. In both models the boundary between the graphene and bulk

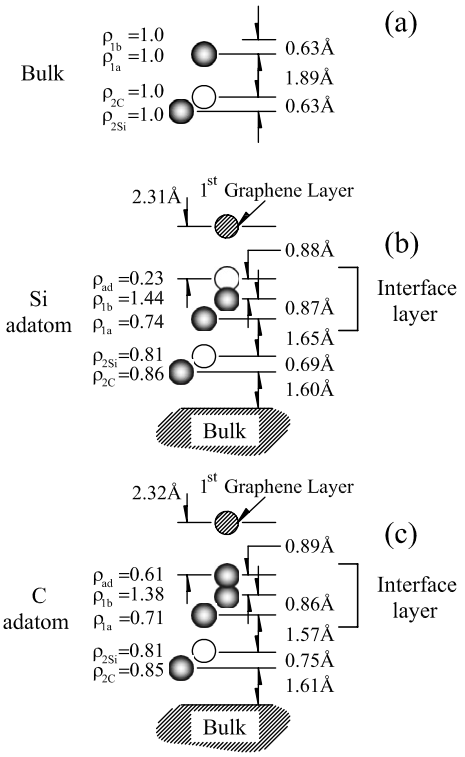


**Figure 21.** Two graphene/SiC interface ball models for graphene grown on the Si-face of SiC determined by surface x-ray reflectivity: (b) Si-adatom model and (c) C-adatom model. Open circles are silicon atoms and shaded circles are carbon atoms. The densities $\rho$ are relative to the densities of bulk SiC shown in (a). From [91].

SiC comprises both density changes and bond relaxation in approximately two bilayers consistent with the XPS conclusions of Johansson *et al* [82]. The two models are distinguished by the structure of the distorted bilayer just below the graphene film. Note that in both models the first graphene layer is $D_0 \sim 2.3$ Å above the interface. This is very large compared the bilayer distance in bulk SiC (1.89 Å) and at the same time much less than the graphite inter-planar spacing of 3.354 Å. This value for $D_0$ is very similar to the value of 2.5 Å measured by STM between a nonconducting layer-0 and a conducting layer-1 [25].

In the C-adatom model a carbon rich layer composed of three carbon planes is sandwiched between the graphene and a slightly distorted SiC bilayer. The total density of these three interface layers is $\rho = 0.61 + 1.38 + 0.71 = 2.70$. This density is substantially lower than the density of a graphene sheet ($\rho = 3.13$) and 30% higher than a bulk SiC bilayer. Note that the bond spacing between the interface layer and the last SiC bilayer is contracted inwards towards the bulk by 0.32 Å giving a substantially smaller Si–C bond length. The Si-adatom model is similar to the C-adatom model in that it also contains a carbon rich layer but composed of two rather than three carbon layers sandwiched between the graphene and the relaxed bilayer. The total density of the interface layers is $\rho = 1.44 + 0.74 = 2.18$, similar to the total bulk bilayer density ($\rho = 2.0$). Atop this layer is a low density of Si atoms. The real distinguishing feature of these two models is the Si atom concentration. Based on the XPS experiments of Johansson *et al* [82], it appears that this model is closer to the actual interface structure.

The high carbon densities in both models suggest a complicated bonding geometry that must contain a mixture of $sp^2$ and $sp^3$ bonded carbon. This assumption is consistent with recent XPS and angle resolved photoemission spectroscopy (ARPES) experiments. Emtsev *et al* [125] have correlated their XPS data with ARPES results. At 1150 °C, when the $6\sqrt{3}$ is well developed and the $\sqrt{3}$ spots have disappeared, they detect the formation of $\sigma$-bands (indicative of $sp^2$ bonding) that are slightly shifted in energy from graphitic $\sigma$-bands that are present after the first graphene layer (layer 1) has formed. The $\pi$-bands do not appear until the surface has been annealed to a higher temperature (1250–1300 °C).

The structural model for the Si-face graphene/SiC interface that emerges from these various experiments, although not complete, has a number of definite features. First, there is an interfacial region with the $6\sqrt{3}$ periodicity between the bulk SiC and the graphene film similar to layer-0 in figure 19. This $(6\sqrt{3} \times 6\sqrt{3})$R30 reconstruction that exists before graphene forms persists with some structural alteration after graphitization. The second common feature is that interface layer-0 is carbon rich with some Si adatoms, possibly in the form of tetramers. The high carbon density and the observed C(1s) core level shifts, along with band structure measurements, suggest that the carbon is in a mixture of $sp^2$ and $sp^3$ bonding. Above this interface, carbon with a graphitic structure begins to grow. While the structure of the Si-face graphene/SiC interface is becoming clear, theoretical and experimental studies to understand the implications of this structure on the electronic properties of this system have also made progress.

The electronic properties of the interface, and the subsequent graphene that grows, have been the subject of numerous studies, some of which reach conflicting conclusions. Here again, however, more detailed experimental studies and theoretical calculations are pointing to a consensus of how these films behave electronically. In particular the role of the graphene substrate interaction and its electronic effects on the first graphene layer are particularly important.

ARPES experiments have measured the band structure of Si-face graphene films [126, 127]. Dispersion curves that correspond to both a single isolated graphene sheet and to multilayer AB... stacked graphene have been measured. Figure 22 shows ARPES data from Ohta *et al* [127] for graphene films of different thickness grown on the Si-face of SiC. It is important to remember that Ohta *et al* have assigned the film thickness in figure 22 by the theoretical band structure signature of $N$ graphene monolayers (see figures 3(a) and 4). Whether or not the linear dispersion they assign as 1 ML comes from a structurally single or double graphene layer cannot be determined by ARPES alone. Regardless, it is clear from figure 22(a) that the linear dispersion at the K-point indicates that the graphene in at least part of the surface behaves electronically like an isolated graphene sheet. Ohta *et al* [28] have attempted to correlate LEEM images from graphitized Si-face samples with ARPES band structure

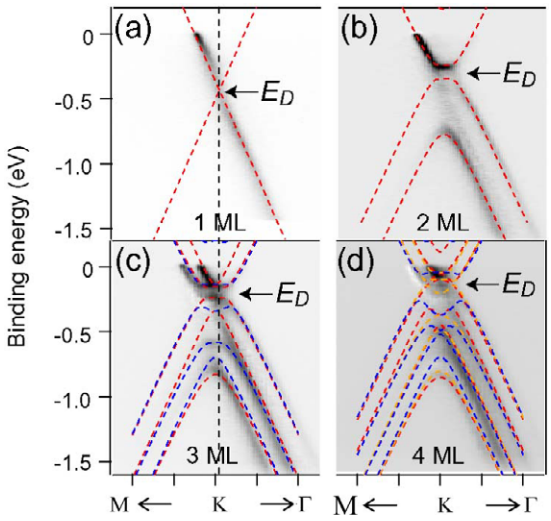


**Figure 22.** ARPES band structure of the $\pi$ and $\pi^*$ bands near $E_F$ and $k_\parallel = -1.703$ Å$^{-1}$ corresponding to graphene's K-point. (a)–(d) data that correspond to the band structure of 1–4 graphene layers, respectively. The dashed lines are from a calculated tight binding band structure, with band parameters adjusted to reproduce measured bands. Light gray (red and orange) lines are for Bernal-type (AB . . . and ABAC . . .) stacking, while dark gray (blue) lines are for rhombohedral-type stacking. Reproduced with permission from [127]. Copyright 2007 by the American Physical Society.

measurements. Given the size of the photoemission beam and the large variation in graphene thickness over micron lengths seen in their LEEM images, as well as similar variations seen by others [92, 112], it would be difficult to separate spectra from regions with zero and one graphene layers.

Early STM measurements attempted to identify the first graphene layer that behaved 'electronically' like an isolated graphene layer by determining whether or not all six atoms in the hexagon could be imaged [23, 94, 120]. As mentioned in the beginning of this section such interpretations of STM images are unreliable for determining the electronic symmetry of a graphene layer. Rutter *et al* [93] have shown with STM and STS that a two layer graphene film above the $(6\sqrt{3} \times 6\sqrt{3})$R30 interface structure is electronically equivalent to Bernal stacked graphene [93]. Whether or not the first graphene layer above the interface layer-0 behaves electronically like isolated graphene has not been definitively proven. STS measurements on graphene layer-1 find a linear dispersion down to 100 meV above the Dirac point, consistent with an isolated sheet, but the possibility of a band gap less than 100 meV cannot be ruled out [93]. Taken in conjunction with the ARPES data in figure 22, the STS and STM clearly show that at least one layer of graphene behaves like an isolated sheet implying that the graphene substrate interaction must be mediated in a way that preserves the equivalence of the A and B sublattices. Such an effect has been theoretically predicted.

One of the first *ab initio* electronic calculations of the graphene/SiC interface was performed by Varchon *et al* [20] They started with one or more graphene layers placed on a bulk terminated SiC surface. Because a full calculation on the large $(6\sqrt{3} \times 6\sqrt{3})$R30 cell are unreasonably long, they used a smaller $(\sqrt{3} \times \sqrt{3})$R30 cell by artificially relaxing the in-plane SiC bond length for both the Si-face and the C-face [20]. A similar calculation by Mattausch and Pankratov was also performed [128] while calculations on a larger $(2\sqrt{3} \times 2\sqrt{3})$R30 cell (with a correspondingly smaller strain) have also been carried out [25]. None of these calculations were intended to accurately describe the interface layer. Indeed the simple model used in these calculations of graphene sitting above a relaxed bulk bilayer is inconsistent with SXRD measurements. Nonetheless the calculations do predict a number of important results. First, the relaxed distance between the last substrate atom and the first graphene layer is larger on the Si-face (2.0 Å) than on C-face graphene. Table 4 compares the Si-face and C-face graphene/substrate bond distance and calculated values from different groups.

**Table 4.** Comparison of the graphene interface layer distances, $D_0$, between graphene grown on 4H–SiC(0001) Si-face and $(000\bar{1})$ C-face.

| | Experimental $D_0$ (Å) | | Theoretical $D_0$ (Å) | |
|---|---|---|---|---|
| Surface | X-ray[a] | STM[b] | $\sqrt{3}$ cell | $2\sqrt{3}$ cell |
| Si-face | 2.30 | 2.5 | 2.0[c], 2.0[d] | 2.0 and 3.4[b] |
| C-face | 1.61 | — | 1.66[c], 1.87[d] | — |

[a] Si-face from [112], C-face from [21].
[b] STM results from [25].
[c] From [20].
[d] From [128].

Another important result from these *ab initio* calculations is the evolution of the band structure with the number of graphene layers [20, 128]. The calculated band structures for graphene on both the Si-face and C-face of SiC are shown in figure 23. The first graphene layer, which is more tightly bound to the substrate, has a significant distortion of the $\pi$-bands that gives rise to a gap in the band structure. This first graphene layer shows no evidence of a graphitic electronic nature. It is not until the second graphene layer that the linear dispersion at the K-point (Dirac cones) characteristic of an isolated graphene sheet develops. Thus, in these calculations, the first graphene layer on both substrates acts as a 'buffer' layer electrically isolating the second graphene layer from the substrate. The third graphene layer shows a splitting of the hole and electron states at the K-point consistent with an AB . . . stacked graphene bilayer [35]. Experimentally there must be a buffer layer to give rise to the linear dispersion in the ARPES measurements. However, it is not clear that the first graphene layer above the interface is this buffer. The STS results in figure 20(c) indicate that the first graphene layer does not have a gap. Brar *et al* [94], on the other hand, see a gap-like feature in the same layer that they could not explain. It is more likely that the interface layer-0 plays the role of the theoretical buffer graphene layer but more work remains before this can be definitively established.

There is one more result of these *ab initio* calculations that is worth noting. For both Si- and C-face surfaces the calculations predict a nearly non-dispersing band near $E_F$ (see figure 23). These states are due to dangling bonds at the graphene substrate interface. The exact position and dispersion of these states, and how they affect the Dirac dispersion, cannot

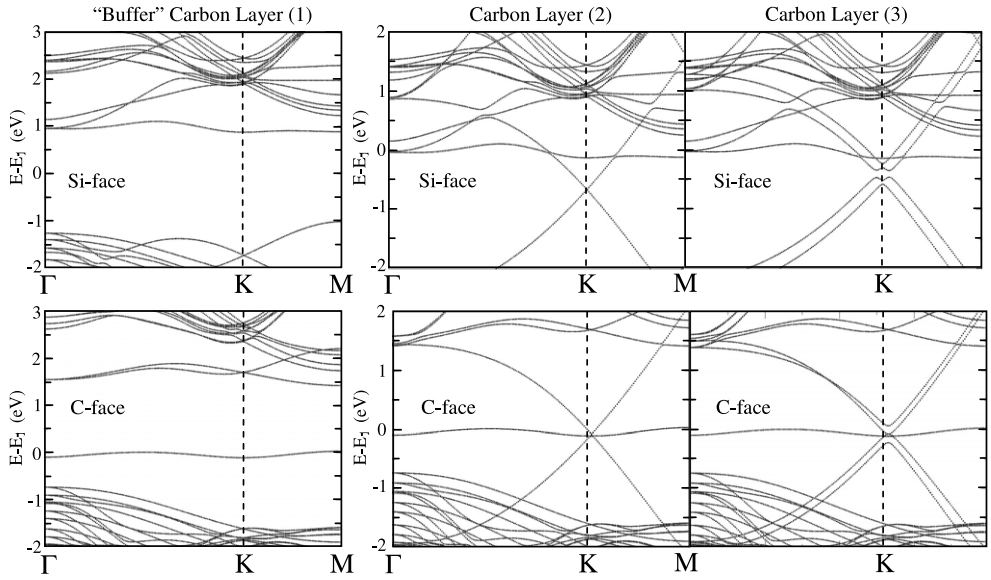


**Figure 23.** Calculated band structure for different numbers of graphene layers on both the Si-face and the C-face of SiC. Reproduced with permission from [20]. Copyright 2007 by the American Physical Society.

be determined by these simple models of the interface because they depend on the exact bonding geometry between the graphene and the interface layer. Nevertheless, it is important to remember that these states do exist and will play a role in the charge transfer between graphene and the SiC interface.

*4.1.2. C-face structure.* From the first discovery of UHV epitaxial graphene growth on C-face SiC it has been known that LEED images show an azimuthal streaking at the graphene rod spacing [54]. Figure 24 shows a detailed LEED image of a multilayer graphene film on a furnace grown C-face sample. Besides the graphene diffraction spots (rods) that are oriented $\phi \pm 30°$ relative to the SiC $[10\bar{1}0]$ direction, the LEED shows a diffuse ring near $\phi = 0.0°$ relative to the SiC $[10\bar{1}0]$ direction that has a radius equal to the reciprocal lattice spacing of graphite. This diffuse structure will be discussed in section 4.2. Since these first experiments, direct structural studies of the graphene/SiC$(000\bar{1})$ system have been limited. Early STM [104] studies of UHV grown C-face graphene and TEM studies [105–107] of furnace grown C-face graphene were more concerned with the origin of CNT formation than graphene growth. However, once the transport properties of these EG films were measured, direct structural studies of this system were reinvigorated. Most of the structural information for C-face films come from SXRD studies of furnace grown EG [21, 27, 129]. The SXRD work in conjunction with earlier spectroscopic studies [61] has begun to shed light on this unique system.

SXRD studies of graphene grown in the C-face of SiC reveal a number of important structural properties including the interface structure and the stacking order of multilayer graphene films. X-ray reflectivity measurements from furnace grown C-face graphene suggest two similar model structures for the interface region between the SiC bulk and the graphene: the 'C-corrugated' and 'C-rich' models shown in figures 25(b) and (c) [21]. In both models the last SiC bilayer immediately

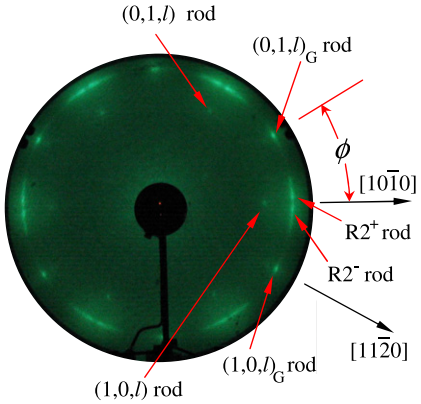


**Figure 24.** LEED image acquired at 72.2 eV from 4H–SiC$(000\bar{1})$ C-face with ~10 graphene layers, showing the graphene and SiC spots and the diffuse arcs labeled as the R2$^+$ and R2$^-$ rods. The SiC $[10\bar{1}0]$ ($\phi = 0$) and $[11\bar{2}0]$ directions are shown for reference.

above the bulk (see figure 19) remain more 'bulk-like' than the corresponding layer for graphene grown on the Si-face. Within measurement errors, both the densities and the atomic spacings in this layer are essentially the same as in the bulk (see figure 25(a)). Like Si-face graphene, the interface layer between the graphene and last bulk layer is significantly different than a bulk bilayer. In other words, both models are consistent with a sharp interface between the graphene and the bulk that is limited to a single reconstructed bilayer. This is unlike extended interface models previously conjectured from electron attenuation arguments [54, 56, 130].

It is the structure of the interface layer-0 that distinguishes the two models. In the C-corrugated model (see figure 25(b)) the interface layer is contracted inwards towards the last bulk layer by 0.11 Å to give a Si–C bond length (1.78 Å) that is slightly smaller than the spacing between bulk bilayers. The interface layer is buckled into three atomic planes: a Si plane

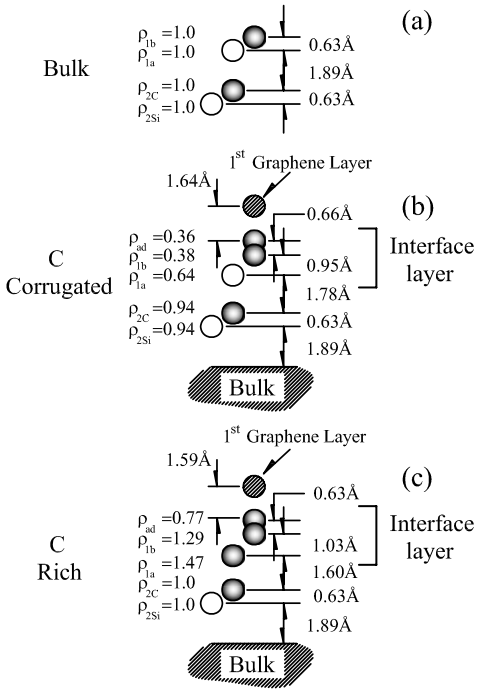


**Figure 25.** Schematic ball models of (a) bulk, (b) C-corrugated and (c) C-rich interface layers between the substrate and the graphene film. Shaded circles are carbon atoms and open circles are silicon atoms. Hatched atoms are carbon atoms in the first graphene layer. Inter-layer spacings and densities (relative to bulk SiC) are shown.

with density $\rho_{1a} = 0.64$ and two nearly equal density carbon planes $\rho_{ad} \approx \rho_{1b}$. Note that the density of both the Si atoms and the sum of the buckled carbon atoms in this interface ($\rho_{ad}+\rho_{1b}$) are each $\sim 2/3$ of the bulk value ($\rho_{bulk} = 1$).

The 'C-rich' model (figure 25(c)) has no Si atoms in the interface layer. The spacing between the last bulk layer and the interface layer (1.60 Å) is considerably shorter than the spacing between bilayers in bulk SiC. Also, the densities of Si and C in the interface layer are higher than a bulk bilayer. Note that the total density of the interface layer is $\rho = 1.47 + 1.29 + 0.77 = 3.53$. This density is $\sim$12% larger than the density of a graphene sheet ($\rho_G = 3.13$). Note also that the $1a$ carbon layer has a density close to the atom density of a (111) diamond plane and a C–C spacing of 1.6 Å, slightly larger than the bond length of diamond (1.54 Å) [131]. This suggests that the interface layer can be viewed as a distorted graphene sheet with a mixture of $sp^2$ and $sp^3$ bonded carbon.

While x-ray diffraction alone cannot distinguish between these two models, the structure of the C-rich graphene/SiC interface is more compelling for several reasons. First, the C-rich model is consistent with XPS experiments [60] that estimate the interface density to be equivalent to four carbon layers. Also, KRIPES measurements [61] deduce that the C-face is more carbon rich than the Si-face. A comparison with the Si-face structures in figure 21 shows that only the C-rich model for the C-face graphene is more carbon rich than either of the two Si-face interface models.

SXRD measurements [21] also show that the first graphene layer grown on the C-face of SiC is very close to the interfacial boundary for both models in figure 25 (the measured average of both models is 1.61 Å). The short bond distance suggests a much stronger graphene–substrate interaction than the van der Waal's bond between graphene planes. Note that the C-face graphene/interface distance is $\sim$0.7 Å closer than the distance measured on Si-face graphene (see table 4). This difference between the two surfaces is consistent with KRIPES experiments. Forbeaux *et al* [62] have shown that, although the graphene $\sigma$ bonds develop at the same temperature for both surfaces, the graphene $\pi^*$ bands visible in the first stage of graphitization (1150 °C) for Si-face graphene are nearly absent on the C-face in spectra taken at a similar temperature (1100 °C). This would be expected if the graphene on the C-face is closer to the interface layer so that the out-of-plane $\pi$ bonds interact with carbon atoms in the interface. The implication of the first graphene layer being tightly bound to the substrate are the same as Si-face grown graphene.

Model calculations by Varchon *et al* [20] of graphene grown on an idealized slightly relaxed SiC surface predict a short SiC first graphene layer bond that is within 15% of the measured value (see table 4). Similar to Si-face graphene, the large charge transfer between the substrate and the first graphene layer grown on the C-face causes a gap in the band structure with no evidence of a graphitic electronic nature. This graphene 'buffer' layer preserves the linear dispersion at the K-point in the second graphene layer as shown in figure 23. Because the calculation does not incorporate the dense distorted interface layer found in the SXRD data, it is difficult to identify which layer in the x-ray model is the buffer. In fact it is likely that the distorted interface layer in figure 25(c) is the 'buffer' layer since the bonding to the slightly distorted SiC bilayer below is also short (1.6 Å). Clearly, more refined model calculations will be necessary to sort this out.

### *4.2. Rotational stacking in C-face graphene*

One of the biggest differences between C-face graphene and Si-face graphene is its epitaxial order with respect to the SiC substrate. It was originally thought that the azimuthal streaking in LEED images similar to figure 24 was due to HOPG-type graphite consisting of azimuthally disordered AB . . . stacked domains. However, three pieces of evidence indicated that this is not the case and that the LEED images are, instead, due to an unusual stacking order that is forced by the graphene/substrate interaction.

First, far-infrared transmission measurements [17, 18] on C-face films ranging from 3 to 60 graphene layers paradoxically show that these multilayer films behave like undoped single layer graphene. This is very surprising since graphitic AB . . . stacking breaks the equivalency of the carbon sublattice atoms in a graphene sheet [35, 45]. While AA . . . stacking faults might explain these results, SXRD data from furnace grown C-face have shown that these types of faults are not present in any appreciable fraction in the multilayer film [21]. AA . . . or ABC . . . stacking faults produce inter-layer contraction [33], contrary to the large average graphene inter-layer expansion measured by SXRD [21]. Instead, the

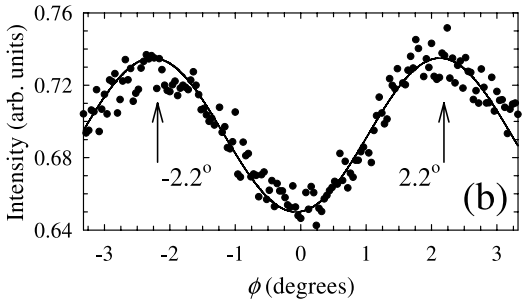


**Figure 26.** X-ray azimuthal scans of the diffuse graphite arc around $\phi = 0$ and $q_{\parallel} = |a_G^*|$ defined in figure 24.

SXRD data suggests rotational faults in the film similar to those in rotationally disordered turbostratic graphite [132]. This type of fault is known to give rise to large inter-layer expansions caused by the interference of $\pi^*$ states between graphene planes [30]. Using a random turbostratic fault model [133], Hass *et al* [21] estimated the probability, $\gamma$, that any two adjacent sheets are faulted to be $\gamma = 0.4$. In other words, after every $1/(1-\gamma) = 1.6$ graphene sheets, a stacking fault occurs in the film.

While the rotational disorder and inter-plane expansion is similar to turbostratic graphene, it must be emphasized that these multilayer graphene films are not turbostratic. Even though turbostratic films can reach domain sizes of up to 1000 Å in the very best samples [134], C-face graphene films are well ordered over much larger distances (see section 3.3.2). In addition, the azimuthal streaking in figure 24 is not random but instead has preferred rotational directions. A close examination of these rings show that they are split. Hass *et al* [129] have looked in more detail at the azimuthal streaking typical in LEED images of C-face grown graphene. X-ray azimuthal scans taken at the radial position of the graphite rod ($|q_{\parallel}| = a_G^*$) around $\phi = 0.0°$ are shown in figure 26. The scan around $\phi = 0.0°$ for this sample shows a diffuse intensity that is peaked at $\phi = \pm 2.2°$.

The significance of the $\pm 2.2°$ preferred rotation is two-fold. First, as shown in table 2, there are three graphene rotations that have nearly commensurate $(6\sqrt{3} \times 6\sqrt{3})$R30 cells with SiC; sheets rotated 30° and $\pm 2.204°$ to the SiC $[10\bar{1}0]$ direction (these will be referred to as the R30, R2$^-$ and R2$^+$ phases). So while the Si-face graphene grows only in the R30 phase, on the C-face furnace grown samples all three rotational phases exist. In addition to graphene aligning into commensurate angles with the SiC, Kolmogorov and Crespi [135] also pointed out that graphene can also align into commensurate structures with itself. One of these commensurate structures forms by rotating two adjacent graphene sheets by $30° \pm 2.204°$. In other words, the three rotational phases coincide with angles corresponding to both a graphene/SiC and a graphene/graphene commensuration [129]. The commensurate superlattice structure formed by two adjacent sheets rotated by $30° \pm 2.204°$ is a $(\sqrt{13} \times \sqrt{13})_G$R46.10° unit cell. This superlattice is shown in figure 27(a).

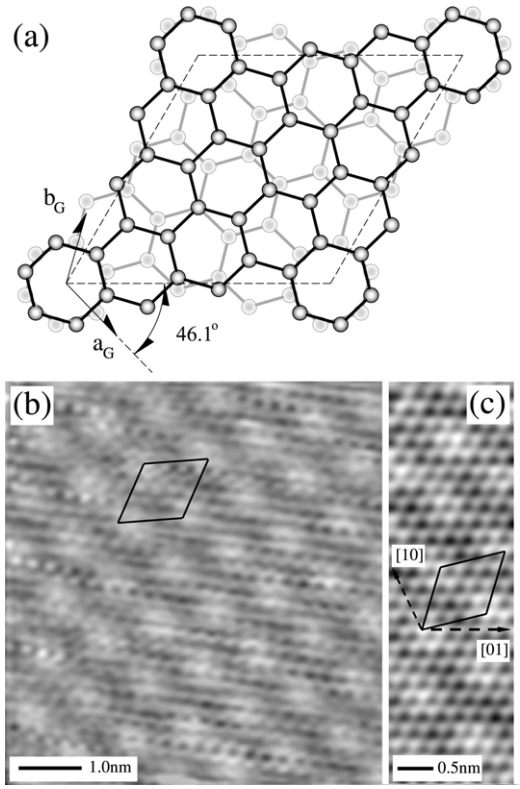


**Figure 27.** (a) Schematic $(\sqrt{13} \times \sqrt{13})_G$R46.1° superlattice formed by a $\beta = 32.204°$ rotated fault pair unit cell (dashed line). Dark circles are R30 graphene atoms ($\mathbf{a}_G$ and $\mathbf{b}_G$ are graphene unit vectors). Gray circles are graphene atoms in the R2$^+$ plane below, rotated 32.204° from the top plane. (b) STM image of C-face graphene showing a periodic superlattice with a $(\sqrt{13} \times \sqrt{13})_G$ cell. (c) High resolution STM image (100 pA constant current, −0.8 V sample bias) of the $(\sqrt{13} \times \sqrt{13})_G$R46.1° unit cell (solid line) and the principle graphene directions (dashed lines). For display, Gaussian smoothing was used in (b) to reduce the atomic corrugation (15–20 pm peak-to-peak in the raw data) relative to the superlattice (∼8 pm peak-to-peak). Reproduced with permission from [129]. Copyright 2008 by the American Physical Society.

There are many other graphene–graphene commensuration angles besides $30° \pm 2.204°$. All commensurate rotations can be calculated when the vector $n\mathbf{a}_G + m\mathbf{b}_G$ in one sheet equals the magnitude of the vector $n_1\mathbf{a}_G + m_1\mathbf{b}_G$ in the second sheet ($n$, $m$, $n_1$ and $m_1$ are integers). Defining $\ell = n^2 + m^2 - nm$, the relative rotation angle $\beta$ of these commensurate sheets is given by:

$$\cos\beta (\mathrm{mod}\ 60°) = \frac{2m_1m + 2n_1n - m_1n - mn_1}{2\ell}. \quad (5)$$

The commensurate structure formed by the rotated sheets is a $(\sqrt{\ell} \times \sqrt{\ell})_G$R$\theta$ unit cell where $\theta$ is the angle between the supercell formed by the rotated pair and the $(1 \times 1)_G$ graphene unit cell. $\theta$ is given by:

$$\cos\theta (\mathrm{mod}\ 60°) = \frac{2m_1 - n_1}{2\sqrt{\ell}}. \quad (6)$$

Remember that a rotation angle of $\beta = 60°$ gives a AB . . . graphene pair. Figure 28 shows a set of commensurate

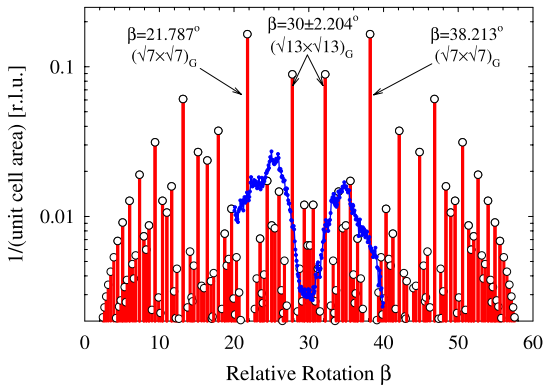


**Figure 28.** Commensurate graphene rotations for $\ell < 64$. The rotations are ranked according to the inverse of their $(\sqrt{\ell} \times \sqrt{\ell})_G R\theta$ unit cell area; $(\ell\sqrt{3}/2)^{-1}$ (circles and drop lines). The $(\sqrt{13} \times \sqrt{13})_G R46.1°$ cell ($\beta = 30° \pm 2.204°$) and the $(\sqrt{7} \times \sqrt{7})_G R49.1°$ cell ($\beta = 30° \pm 8.213°$) are marked. (Red lines and circles) an SXRD experimental distribution of rotations for a 25 layer C-face graphene film (solid line) [112].

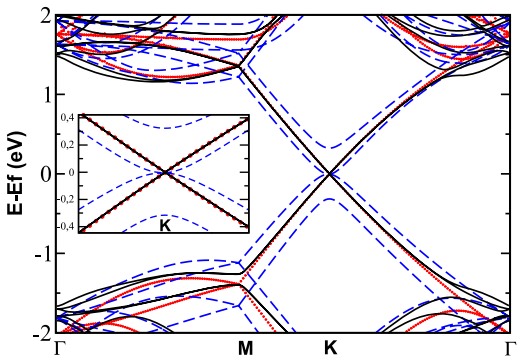


**Figure 29.** Calculated band structure for three forms of graphene. (i) Isolated graphene sheet (dots), (ii) AB . . . graphene bilayer (dashed line) and (iii) R30/R2$^+$ fault pair (solid line). Inset shows details of band structure at the K-point. Reproduced with permission from [129]. Copyright 2008 by the American Physical Society.

rotations when $\ell < 64$. The rotation angles are plotted for display purposes using an arbitrary metric; their inverse unit cell size $(\ell\sqrt{3}/2)^{-1}$. The actual energy cost of these rotated pairs has only been estimated for two of the many commensurate cells: the $(\sqrt{13} \times \sqrt{13})_G R46.1°$ cell and the $(\sqrt{7} \times \sqrt{7})_G R49.1°$ cell in figure 28. Theoretical calculations find that the larger $(\sqrt{13} \times \sqrt{13})_G R46.1°$ cell has the lower energy of the two by about 0.2–0.3 meV/atom [135, 136]. An experimental distribution of rotation angles, measured by SXRD, is shown for comparison [112]. Note that the experimental distribution shows a preference for angles slightly larger and smaller than 30°.

SXRD and STM experiments have shown that multilayer graphene grown on the C-face has a high density of rotational stacking faults consisting of these commensurate graphene sheet pairs [129]. Figures 27(b) and (c) show STM images of $(\sqrt{13} \times \sqrt{13})_G R(\pm 46.1°)$ modulation of the graphene lattice from a C-face film. Further SXRD experiments to determine the stacking structure of C-face films show that the films are not AB . . . stacked. Instead the films contain many rotational fault pairs interleaved in the multilayer graphene film (approximately one fault every 1.6–2.5 layers) [129]. This is consistent with the x-ray reflectivity estimates [21]. The majority of these faults are rotated approximately 30° apart [112].

It is worth noting that STM images similar to figure 27(b) are observed in natural and HOPG graphite after cleaving (note that corrugation amplitudes are typically larger than >10 Å compared to ∼0.1 Å for C-face graphene) [137]. It is conjectured that the energy imparted to the surface during the cleaving process is responsible for causing rotational faults in the top layer. Apparently a highly directional graphene–SiC interaction makes production of these faults more ubiquitous, while maintaining the flatness of the graphene sheets. How this is accomplished is not understood. Assuming that each new C-face graphene layer grows at the SiC/graphene interface as observed for Si-face films, it is possible that stoichiometry changes, as successive SiC bilayers are exposed during graphene growth, act as new angular templates for the next graphene layer. Why rotations of approximately 30° are selected has yet to be determined. It is also possible that SiC step edges influence the growth direction of a graphene layer (this may explain the asymmetry of the experimental distribution of angles in figure 28).

As discussed in section 2.1 the electronic properties of multilayer graphene depend on the stacking order. Therefore the electronic properties of C-face multilayer films should be very different from those of graphite because of the high stacking fault density. For a R30/R2$^{\pm}$ fault pair in figure 27(a) there are only 2 atoms/sheet out of 52 in the $(\sqrt{13} \times \sqrt{13})_G R(\pm 46.1°)$ cell that are in high symmetry positions, i.e. atom-over-atom sites. This suggests weak inter-planar interactions in the fault pairs that help to preserve the symmetry of the graphene sheet [26, 123, 129]. Figure 29 compares *ab initio* band structure calculations [129] for an isolated graphene sheet, a graphene bilayer with Bernal AB . . . stacking and the bilayer rotational fault pair of figure 27(a). The $\Gamma$ $K$ $M$ direction shown is the $(\sqrt{13} \times \sqrt{13})_G R \pm 46.1°$ cell high symmetry direction. The main differences in the electronic structure of the three graphene forms show up in the dispersion curves near the K-points. The band structure for an isolated graphene sheet shows the linear gapless dispersion of the $\pi$ bands at the K-point. The normal Bernal stacking of graphene breaks the sublattice symmetry, giving rise to splitting of the $\pi$ bands with a corresponding change to a parabolic shape and a lower group velocity [35]. With the rotated fault, the linear dispersion is recovered near the K-points. This dispersion is identical to the graphene dispersion (same Fermi velocity) and clearly shows that in the rotated layers, the atoms in the A and B sublattices are identical.

### *4.3. Thickness determination*

To date, there is no standard procedure for absolute determination of the number of graphene layers present on either polar face of SiC. A number of surface analysis techniques have been employed to measure graphene film thickness. While different methods provide pieces of the puzzle, a comprehensive and comparative study to determine

what is being measured, the relative accuracy of a particular technique and under what conditions each is applicable has yet to be carried out. In this section we attempt to assess and correlate information from all current methods that have been applied to the problem of determining graphene coverage. As previously mentioned, graphene can be defined both structurally and electronically. Because there is no tool that can provide a complete picture of both these properties, it is critical to use more than one technique in order to make sensible conclusions about the morphology of these films. Techniques used to probe graphene's atomic structure include: SXRD, ellipsometry, LEED and LEEM. Techniques entirely based on electronic band structure measurements are KRIPES and ARPES that are capable of probing the type of bonding between atoms. Other techniques like STM, STS, AES, XPS and Raman spectroscopy provide both structural, electronic and local chemical composition.

It must also be kept in mind that all of these techniques, with the exception of STM and LEEM, measure properties averaged over the probe beam size. Because graphene thickness and growth rate are sensitive to temperature, thermal gradients across a sample can produce a lateral height distribution in the graphene film. If the height distribution is wide, an average thickness determined from a spatially averaging probe must be taken with a grain of salt. As a final caveat, measurements of thickness by many of these techniques are heavily dependent on a model of the SiC/graphene system and therefore have systematic errors that are dependent on the accuracy of the model. In many cases it has been assumed that the graphene rests directly above a bulk terminated surface. As shown in section 4.1 this is not correct.

An early method that is still used to determine graphene thickness is AES [2, 60, 63, 81]. The carbon (KLL) AES spectrum shows a distinct change from C in SiC to C in graphene. This is shown in the insert of figure 30. The ratio of the Si(LVV)/C(KLL) peak area can be tracked as the films develop and used as an estimate of the number of graphene layers. Li [81] has calculated the Si(LVV)/C(KLL) ratios, including the appropriate inelastic mean free paths and elemental sensitivity factors, for three different models for graphene grown on the Si-face of SiC (see [81] for details of the calculation).

(1) The graphene films are grown directly on the bulk terminated Si-face of SiC.
(2) A Si interface layer with 1/3 the density of Si in the bulk bilayer. This was used to represent an adatom layer.
(3) The same model as (2) but with C atoms substituted for the Si adatoms.

Note that models (1) and (2) have about 1/8 the density of atoms in the interface layer as determined by SXRD (see figure 21). This means that AES measurements, based on the above model, will overestimate the film thickness by ∼1 layer because the experimental C(KLL) intensity includes a contribution from the dense non-graphitic interface carbon layer in figure 21. Besides choosing the appropriate model, there are a number of other factors that must be considered in applying AES to determine graphene thickness. Because

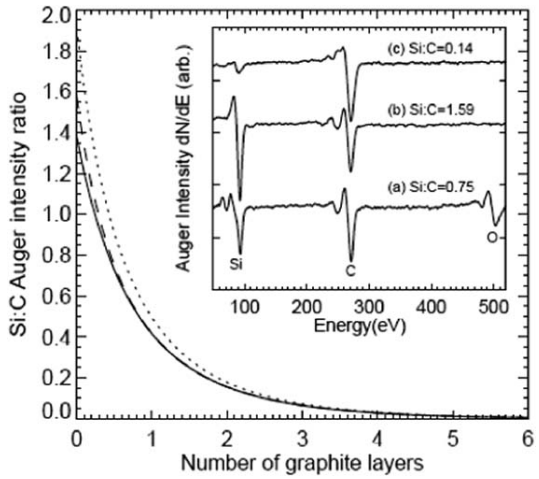


**Figure 30.** The number of estimated graphene layers versus Auger peak-to-peak ratio of the Si(LVV)/C(KLL) lines for the three models: (I) bulk terminated SiC (dash line), (II) A Si-adatom interface with 1/3 the bulk atom density (dotted line), (III) A C-adatom interface with 1/3 the bulk atom density (solid line). The inset show Auger spectra corresponding to different Si-face reconstructions after heating in UHV. (a) clean surface after $H_2$ etching, (b) $(\sqrt{3} \times \sqrt{3})$R30 surface after annealing to 1150 °C, (c) Graphitized $(6\sqrt{3} \times 6\sqrt{3})$R30 surface after annealing to 1350 °C.

the electron penetration depth of the Si(LVV) electron is short, AES estimates becomes very uncertain for graphene layers exceeding more than four layers. This makes the AES method more applicable to Si-face films than to the thicker C-face graphene films. The AES estimate also depends on the growth process. For instance, if the growth leaves an excess of Si atoms on the surface, the AES method is seriously compromised and will underestimate the number of graphene layers.

The AES model given above has been compared to SXRD measurements. SXRD measures the graphene layer thickness two ways: (i) by measuring the specular reflectivity and (ii) by measuring the crystal truncation rods of graphene [138, 139]. Method (i) gives the density gradient vertical to the surface (including the interface layer) and allows for a weighted average of film thicknesses over the beam size. Method (ii) is only sensitive to the number of crystallographic graphene layers but because of the grazing incidence geometry the results represent an average over millimeter dimensions. Figure 31 shows the layer height histogram for a UHV grown Si-face graphene film as determined by x-ray reflectivity. The average number of graphene layers is 1.9 ± 1.5. The distribution is very wide, in part reflecting the 3 mm spatial average of the x-ray beam. In particular the high areal fraction not covered by graphene (18%) can be associated with cooler areas near the edge of the sample caused by non-uniformity in the e-beam heater. AES measurements on the same sample estimate the graphene coverage at 3.2 layers, consistent with the lack of a realistic interface layer in the AES calculation described above. In general AES, using the model of [81], overestimates the number of graphene layers by one to two layers [91, 112].

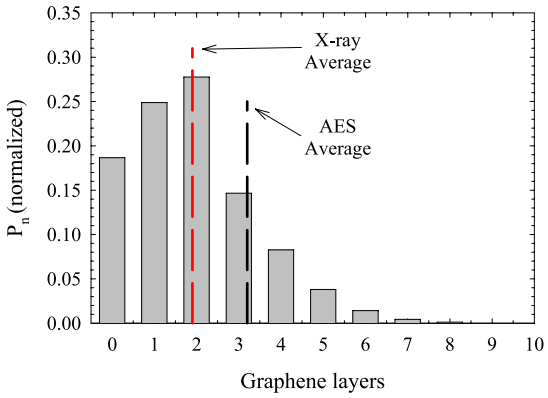


**Figure 31.** The normalized probability, $P(n)$, of a $n$-graphene layer stack from a UHV grown Si-face film was determined by x-ray reflectivity. The x-ray average is $1.9 \pm 1.5$ graphene layers while the AES estimate is slightly more than one layer thicker (3.2 layers). From [91].

XPS has also been extensively used to study the graphene/SiC system and like AES it suffers from the same errors in estimates of the number of graphene layers [22, 60, 82, 89, 113]. The C(1s) photoemission spectrum shows a binding energy shift from C in SiC to C in graphitic structures. The relative intensities of the graphitic C(1s) and the SiC C(1s) peaks can be used to estimate graphene thickness. A similar estimate can be made by comparing the relative intensities of the Si(2p) and C(1s) peaks [22, 89]. Once again the estimates are based on a simple model of a bulk terminated substrate, so we expect these thickness estimates to be 1–2 layers thicker than the actual number of layers.

Ellipsometry is another technique that has been used to estimate the number of graphene layers. It is based on a model for the change in the optical polarization of incident visible light reflected from the surface [68]. The beam size is typically 200 $\mu$m but is elongated due to the incident angle. This technique probes the surface on a millimeter scale. The technique is based on four wavelength dependent optical constants ($n_o$, $n_e$, $k_o$ and $k_e$) of the film and the SiC. The reflected beam is a coherent sum of beams reflected from the SiC/graphene interface and the graphene/air interface. In principle the technique can measure film thicknesses from less than 1 layer up to $10^3$ layers [68]. Its accuracy, as applied to epitaxial graphene, primarily depends on the reliability of the optical constants of graphene, which vary significantly in the literature. The best set of data for a range of energies from 2–5 eV appears to be by Jellison *et al* [140]. Using a model of a bulk terminated SiC substrate, we have compared ellipsometry thickness measurements to AES and SXRD measurements [112]. Like AES, ellipsometry predicts an average of 1–2 extra graphene layers compared to SXRD estimates. The advantages of ellipsometry over AES are that surface segregated Si has less of an effect on the graphene thickness estimate and is not limited to measurements of films less than 4–5 layers.

LEEM [141] has recently been used to study the graphene films grown on the Si-face of SiC [28, 92]. LEEM is a direct space imaging technique that has a spatial resolution down to 50 $\mu$m. The number of graphene layers are determined by using quantized oscillations in the low energy electron reflectivity. Because of these oscillations, the LEEM intensity at a fixed incident electron energy will change with layer thickness giving the spatial contrast required to see regions of different height [142]. LEEM has sufficient contrast to distinguish between a graphene layer and the $(6\sqrt{3} \times 6\sqrt{3})$R30 layer. Because LEEM is a direct space imaging technique, it can directly measure the spatial variation of graphene film thickness over many microns. Hibino *et al* [92] see graphene height variations on UHV grown Si-face graphene that range from one to seven layers over a 2000 Å $\times$ 2000 Å field of view. This variation is similar to that measured by SXRD (see figure 31).

## 5. Conclusion

Epitaxial graphene electronics is in its infancy, yet many early milestones in epitaxial graphene research have opened the way to promising applications of this material. There are a number of important aspects of epitaxial graphene that this review has attempted to highlight. First, the structure and growth of epitaxial graphene are very different on the two polar faces of hexagonal SiC: the (0001) and (000$\bar{1}$). These differences have been overlooked in the literature for some time. Their implications are only now coming to light. Second, significant improvements in the growth of epitaxial graphene on hexagonal SiC have been demonstrated. This is particularly true for graphene films grown on the SiC(000$\bar{1}$) surface that are now reaching dimensions larger than can be easily measured. These films are fast approaching wafer-scale dimensions meaning that they are now being characterized by the yield of operational switching devices per mm$^2$ instead of domain sizes in units of $\mu$m$^2$. Further improvements are expected once the growth kinetics of these films are understood. Besides improvements in growth, structural studies have been able to explain a number of unusual electronic properties of these films. Even though the details of the graphene–substrate interface structure are still not completely known, both experiment and theory agree that substrate interaction are buffered so that the graphene symmetry is preserved for at least one graphene layer. This explains why epitaxial graphene can have electronic properties like an isolated graphene sheet. The Schottky barrier between the metallic graphene layer and the semiconducting interface influence doping of the graphene. Because the properties of this barrier will depend on the structure and passivation of the interface layer, active research on the structure and electronic properties of this layer is expected. On the SiC(000$\bar{1}$) surface the unusual rotational stacking in multilayer graphene explains why these films behave like isolated graphene sheets even when they are stacked up to 60 layers. We expect an explosion of research that will exploit these properties for new and unusual epitaxial graphene devices.

## Acknowledgments

We would like to thank C Berger and A Zangwill for their critical reading of this review and P N First for many fruitful

discussions. We are also grateful to M Sprinkle, G Rutter and J A Stroscio for both making suggestions to this review and for providing us access to their unpublished figures. We also wish to give special thanks to M Hupalo and M Tringides for giving us advanced copies of their manuscript on Si-face graphene processing as well as permission to use their figures.

## References

[1] Berger C *et al* 2004 *J. Phys. Chem.* B **108** 19912
[2] Berger C *et al* 2006 *Science* **312** 1191
[3] Nakada K, Fujita M, Dresselhaus G and Dresselhaus M S 1996 *Phys. Rev.* B **54** 17954
[4] Wakabayashi K, Fujita M, Ajiki H and Sigrist M 1999 *Phys. Rev.* B **59** 8271
[5] Son Y-W, Cohen M L and Louie S G 2006 *Phys. Rev. Lett.* **97** 216803
[6] Novoselov K S, Geim A K, Morozov S V, Jiang D, Zhang Y, Dubonos S V, Grigorieva I V and Firsov A A 2004 *Science* **306** 666
[7] Zhang Y, Tan Y-W, Stormer H L and Kim P 2005 *Nature* **438** 201
[8] Novoselov K S, Geim A K, Morozov S V, Jiang D, Katsnelson M I, Grigorieva I V, Dubonos S V and Firsov A A 2005 *Nature* **438** 197
[9] Geim A K and Novoselov K S 2007 *Nat. Mater.* **6** 183
[10] Zhang Y, Small J P, Pontius W V and Kim P 2005 *Appl. Phys. Lett.* **86** 073104
[11] Zhang Y, Small J P, Amori E S and Kim P 2005 *Phys. Rev. Lett.* **94** 176803
[12] Bunch J S, Yaish Y, Brink M, Bolotin K and McEuen P L 2005 *Nano. Lett.* **5** 287
[13] Novoselov K S, Jiang D, Schedin F, Booth T J, Khotkevich V V, Morozov S V and Geim A K 2005 *Proc. Natl Acad. Sci. USA* **102** 10451
[14] de Heer W A *et al* 2007 *Solid State Commun.* **143** 92
[15] Wu X, Li X, Song Z, Berger C and de Heer W A 2007 *Phys. Rev. Lett.* **98** 136801
[16] Ando T, Nakanishi T and Saito R 1998 *J. Phys. Soc. Japan* **67** 2857
[17] Sadowski M L, Martinez G, Potemski M, Berger C and de Heer W A 2006 *Phys. Rev. Lett.* **97** 266405
[18] Sadowski M L, Martinez G, Potemski M, Berger C and de Heer W A 2007 *Solid State Commun.* **143** 123
[19] Ohta T, Bostwick A, Seller T, Horn K and Rotenberg E 2006 *Science* **313** 951
[20] Varchon F *et al* 2007 *Phys. Rev. Lett.* **99** 126805
[21] Hass J, Feng R, Millán-Otoya J E, Li X, Sprinkle M, First P N, Berger C, de Heer W A and Conrad E H 2007 *Phys. Rev.* B **75** 214109
[22] Rollings E, Gweon G-H, Zhou S Y, Mun B S, McChesney J L, Hussain B S, Fedorov A V, First P N, de Heer W A and Lanzara A 2006 *J. Phys. Chem. Solids* **67** 2172
[23] Mallet P, Varchon F, Naud C, Magaud L, Berger C and Veuillen J-Y 2007 *Phys. Rev.* B **76** 041403(R)
[24] Rutter G M, Crain J N, Guisinger N P, Li T, First P N and Stroscio J A 2007 *Science* **317** 219
[25] Rutter G M, Guisinger N P, Crain J N, Jarvis E A A, Stiles M D, Li T, First P N and Stroscio J A 2007 *Phys. Rev.* B **76** 235416
[26] Lopes dos Santos J M B, Peres N M R and Castro Neto A H 2007 *Phys. Rev. Lett.* **99** 256802
[27] Hass J, Feng R, Li T, Li X, Song Z, de Heer W A, First P N, Conrad E H, Jeffrey C A and Berger C 2006 *Appl. Phys. Lett.* **89** 143106
[28] Ohta T, El Gabaly F, Bostwick A, McChesney J, Emtsev K V, Schmid A K, Seyller T, Horn K and Rotenberg E 2007 *Preprint* 0710.0877[cond-mat.mtrl-sci]
[29] Kedzierski J, Hsu P-L, Healey P, Wyatt P, Keast C, Sprinkle M, Berger C and de Heer W 2008 *Preprint* 0801.2744[cond-mat.mtrl-sci]
[30] Baskin Y and Mayer L 1955 *Phys. Rev.* **100** 544
[31] Haering R R 1958 *Can. J. Phys.* **36** 352
[32] Schabel M C and Martins J L 1992 *Phys. Rev.* B **46** 7185
[33] Charlier J-C, Gonze X and Michenaud J-P 1994 *Carbon* **32** 289
[34] Wallace P R 1947 *Phys. Rev.* **71** 622
[35] Latil S and Henrard L 2006 *Phys. Rev. Lett.* **97** 036803
[36] Katsnelson M I and Novoselov K S 2007 *Solid State Commun.* **143** 3 and references therein
[37] Slonczewski J C and Weiss P R 1958 *Phys. Rev.* **109** 272
[38] Semenoff G W 1984 *Phys. Rev. Lett.* **53** 2449
[39] Haldane F D M 1988 *Phys. Rev. Lett.* **61** 2015
[40] Peres N M R, Guinea F and Castro Neto A H 2006 *Phys. Rev.* B **73** 125411
[41] Guinea F, Castro Neto A H and Peres N M R 2006 *Phys. Rev.* B **73** 245426
[42] McCann E and Fal'ko V I 2006 *Phys. Rev. Lett.* **96** 086805
[43] Nilsson J, Castro Neto A H, Peres N M R and Guinea F 2006 *Phys. Rev.* B **73** 214418
[44] Koshino M and Ando T 2006 *Phys. Rev.* B **73** 245403
[45] Partoens B and Peeters F M 2006 *Phys. Rev.* B **74** 075404
[46] Frank S, Poncharal P, Wang Z L and de Heer W A 1998 *Science* **280** 1744
[47] Hertel T and Moos G 2000 *Phys. Rev. Lett.* **84** 5002
[48] Klien O 1929 *Z. Phys.* **53** 157
[49] Martino A D, Dell'Anna L and Egger R 2007 *Phys. Rev. Lett.* **98** 066802
[50] Miyamoto Y, Nakada K and Fujita M 1999 *Phys. Rev.* B **59** 9858
Ezawa M 2006 *Phys. Rev.* B **73** 045432
Peres N M R, Castro Neto A H and Guinea F 2006 *Phys. Rev.* B **73** 195411
Brey L and Fertig H A 2006 *Phys. Rev.* B **73** 235411
Ouyang Y, Yoon Y, Fodor J K and Guo J 2006 *Appl. Phys. Lett.* **89** 203107
Son Y-W, Cohen M L and Louie S G 2006 *Nature* **444** 347
Son Y-W, Cohen M L and Louie S G 2006 *Phys. Rev. Lett.* **97** 216803
Barone V, Hod O and Scuseria G E 2006 *Nano Lett.* **6** 2748
Areshkin D A, Gunlycke D and White C T 2007 *Nano Lett.* **7** 204
[51] Han M Y, Özyilmaz B, Zhang Y and Kim P 2007 *Phys. Rev. Lett.* **98** 206805
[52] Bauer A, Kräusslich J, Dressler L, Kuschnerus P, Wolf J, Goetz K, Käckell P, Furthmüller J and Bechstedt F 1998 *Phys. Rev.* B **57** 2647
[53] Bauer A, Reischauer Ph, Kräusslich J, Schell N, Matz W and Goetz K 2001 *Acta Crystallogr.* A **57** 60
[54] Van Bommel A J, Crombeen J E and van Tooren A 1975 *Surf. Sci.* **48** 463
[55] Owman F and Mårtensson P 1995 *Surf. Sci.* **330** L639
[56] Forbeaux I, Themlin J-M and Debever J-M 1998 *Phys. Rev.* B **58** 16396
[57] Rosei R, De Crescenzi M, Sette F, Quaresima C, Savoia A and Perfetti P 1983 *Phys. Rev.* B **28** 1161
Fujita D and Yoshihara K 1994 *J. Vac. Sci. Technol.* A **12** 2134
Pan Y, Jiang N, Sun J T, Shi D X, Du S X, Liu F and Gao H-J 2007 *Preprint* 0709.2858[cond-mat.mtrl-sci]
[58] Obraztsov A N, Obraztsova E A, Tyurina A V and Zolotukhin A A 2007 *Carbon* **45** 2017
[59] Li L and Tsong I S T 1996 *Surf. Sci.* **351** 141
[60] Muehlhoff L, Choyke W J, Bozack M J and Yates J T 1986 *J. Appl. Phys.* **60** 2842
[61] Forbeaux I, Themlin J-M and Debever J-M 1999 *Surf. Sci.* **442** 9

[62] Forbeaux I, Themlin J-M, Charrier A, Thibaudau F and Debever J-M 2000 *Appl. Surf. Sci.* **162/163** 406
[63] Tsukamoto T, Hiria M, Kusaka M, Iwami M, Ozawa T, Nagamura T and Nakata T 1997 *Surf. Sci.* **371** 316
[64] Tsukamoto T, Hiria M, Kusaka M, Iwami M, Ozawa T, Nagamura T and Nakata T 1997 *Appl. Surf. Sci.* **113/114** 467
[65] Xie X N, Lim R, Li J, Li S F Y and Loh K P 2001 *Diamond Relat. Mater.* **10** 1218
[66] Charrier A, Coati A, Argunova T, Thibaudau F, Garreau Y, Pinchaux R, Forbeaux I, Debever J-M, Sauvage-Simkin M and Themlin J-M 2002 *J. Appl. Phys.* **92** 2479
[67] Angot T, Protail M, Forbeaux I and Layet J M 2002 *Surf. Sci.* **502/503** 81
[68] Meyer F and Loyen C J 1975 *Acta Electron.* **18** 33
[69] Pezoldt J, Trushin Y V, Kharlamov V S, Schmidt A A, Cimalla V and Ambacher O 2006 *Nucl. Instrum. Methods Phys. Res.* B **253** 241
[70] Bockstedte M, Mattausch A and Pankratov O 2003 *Phys. Rev.* B **68** 205201
[71] For a review see Li L and Sakurai T 2000 *Advances in Scanning Probe Microscopy* (*Advances in Materials Research Series*) ed T Sakurai and Y Watanabe (Berlin: Springer)
[72] Harris G L (ed) 1995 *Properties of Silicon Carbide* (*EMIS Data Reviews Series* vol 13) (London: INSPEC)
[73] Kaplan R and Parrill T M 1986 *Surf. Sci.* **165** L45
[74] Ramachandran V, Brady M F, Smith A R, Feenstra R M and Greve D W 1997 *J. Electron. Mater.* **27** 308
[75] Xie Z Y, Wei C H, Li L Y, Yu Q M and Edgar J H 2000 *J. Cryst. Growth* **217** 115
[76] Xue Q, Xue Q K, Hasegawa Y, Tsong I S T and Saurai T 1999 *Appl. Phys. Lett.* **74** 2468
[77] Li L, Hasegawa Y, Tsong I S T and Saurai T 1996 *J. Physique* IV **6** 167
[78] Kaplan R 1989 *Surf. Sci.* **215** 111
[79] Li L, Hasegawa Y, Sakurai T and Tsong I S T 1996 *J. Appl. Phys.* **80** 2524
[80] Bermudez V M 1995 *Appl. Surf. Sci.* **84** 45
[81] Li T 2006 *PhD Thesis* Georgia Institute of Technology
[82] Johansson L I, Owman F and Mårtensson P 1996 *Phys. Rev.* B **53** 13793
[83] Heinz K, Starke U, Bernhardt J and Schardt J 2000 *Appl. Surf. Sci.* **162** 9
[84] Starke U, Schardt J, Bernhardt J, Franke M and Heinz K 1999 *Phys. Rev. Lett.* **82** 2107
[85] Starke U, Bram Ch, Steiner P-R, Hartner W, Hammer L, Heinz K and Muüller K 1995 *Appl. Surf. Sci.* **89** 175
[86] Riedl C, Starke U, Franke M and Heinz K 2007 *Phys. Rev.* B **76** 245406
[87] Chang C S, Tsong I S T, Wang Y C and Davis R F 1991 *Surf. Sci.* **256** 354
[88] Chen W, Xu H, Liu L, Gao X, Qi D, Peng G, Tan S C, Feng Y, Loh K P and Wee A T S 2005 *Surf. Sci.* **596** 176
[89] Seyller Th *et al* 2006 *Surf. Sci.* **600** 3906
[90] Gu G, Nie S, Feenstra R M, Devaty R P, Choyke W J, Chan W K and Kane M G 2007 *Appl. Phys. Lett.* **90** 253507
[91] Millán-Otoya J E, Hass J, First P N and Conrad E H 2008 at press
[92] Hibino H, Kageshima H, Maeda F, Nagase M, Kobayashi Y and Yamaguchi H 2008 *Phys. Rev.* B **77** 075413
[93] Rutter G M, Crain J N, Guisinger N P, First P N and Stroscio J A 2008 *J. Vac. Sci. Technol.* at press
[94] Brar V W, Zhang Y, Yayon Y, Ohta T, McChesney J L, Bostwick A, Rotenberg E, Horn K and Crommie M F 2007 *Appl. Phys. Lett.* **91** 122102
[95] Hupalo M, Conrad E H and Tringides M 2008 at press
[96] Bernhardt J, Schardt J, Starke U and Heinz K 1999 *Appl. Phys. Lett.* **74** 1084
Starke U, Schardt J, Bernhardt J and Heinz K 1999 *J. Vac. Sci. Technol.* A **17** 1688
[97] Johansson L I, Glans P-A and Hellgre N 1998 *Surf. Sci.* **405** 288
[98] Bernhardt J, Nerding M, Starke U and Heinz K 1999 *Mater. Sci. Eng.* B **61** 206
[99] Seubert A, Bernhardt J, Nerding M, Starke U and Heinz K 2000 *Surf. Sci.* **454** 45
[100] Hoster H E, Kulakov M A and Bullemer B 1997 *Surf. Sci.* **382** L658
[101] Nishimori K, Tokutaka H, Nakanishi S, Kishida S and Ishihara N 1989 *Japan. J. Appl. Phys.* **28** L1345
[102] Nakanishi S, Tokutaka H, Nishimori K, Kishida S and Ishihara N 1989 *Appl. Surf. Sci.* **41/42** 44
[103] Badziag P 1990 *Surf. Sci.* **236** 48
[104] Naitoh M, Kitada M, Nishigaki S, Toyama N and Shoji F 2003 *Surf. Rev. Lett.* **10** 473
[105] Kusunoki M, Suzuki T, Kaneko K and Ito M 1999 *Phil. Mag. Lett.* **79** 153
[106] Maruyama T, Bang H, Fujita N, Kawamura Y, Naritsuka S and Kusunoki M 2007 *Diamond Relat. Mater.* **16** 1078
[107] Kusunoki M, Suzuki T, Hirayama T, Shibata N and Kaneko K 2000 *Appl. Phys. Lett.* **77** 531
[108] Sprinkle M, Berger C and de Heer W A 2008 at press
[109] Sharma N 2008 *PhD Thesis* Georgia Institute of Technology at press
[110] Pimenta M A, Dresselhaus G, Dresselhaus M S, Cançado L G, Jorioa A and Saitoe R 2007 *Phys. Chem. Chem. Phys.* **9** 1276
[111] Ferrari A 2007 *Solid State Commun.* **143** 47
[112] Hass J 2008 *PhD Thesis* Georgia Institute of Technology, at press
[113] Ong W J and Tok E S 2006 *Phys. Rev.* B **73** 045330
[114] Ma Y 2007 Simulation of interstitial diffusion in graphite *Phys. Rev.* B **76** 075419
[115] Matsunami H 2004 Technological breakthroughs in growth control of silicon carbide, for high power electronic devices *Japan. J. Appl. Phys.* **43** 6835
[116] Irle S, Wang Z, Zheng G, Morokuma K and Kusunoki M 2006 *J. Chem. Phys.* **125** 044702
[117] Meyer C, Geim A K, Katsnelson M I, Novoselov K S, Booth T J and Roth S 2007 *Nature* **446** 60
[118] Viculis L M, Mack J J and Kaner R B 2003 *Science* **299** 5611
Viculis L M, Mack J J, Mayer O M, Hahn H T and Kaner R B 2005 *J. Mater. Chem.* **15** 9
Niyogi S, Bekyarova E, Itkis M E, McWilliams J L, Hammon M A and Haddon R C 2006 *J. Am. Chem. Soc.* **128** 1720
Stankovich S, Dikin D A, Dommett G H B, Kohlhass K M, Zimmey E J, Stach E A, Piner R D, Nguyen S B T and Ruoff R S 2006 *Nature* **442** 282
Stankovich S, Piner R D, Chen X, Wu N, Nguyen T and Ruoff R S 2006 *J. Mater. Chem.* **16** 155
[119] Mermin N D and Wagner H 1966 *Phys. Rev. Lett.* **17** 1133
[120] Stolyarova E, Rim K T, Ryu S, Maultzsch J, Kim P, Brus L E, Heinz T F, Hybertsen M S and Flynn G W 2007 *Proc. Natl Acad. Sci.* **104** 9209
[121] Faugeras C, Nerrière A, Potemski M, Mahmood A, Dujardin E, Berger C and de Heer W A 2008 *Appl. Phys. Lett.* **92** 011914
[122] Atamny F, Spillecke O and Schlögl R 1999 *Phys. Chem. Chem. Phys.* **1** 4113
[123] Latil S, Meunier V and Henrard L 2007 *Phys. Rev.* B **76** 201402

[124] Grass M, Fischer D, Mathes M, Gantefor G and Nielaba P 2002 *Appl. Phys. Lett.* **81** 3810
[125] Emtsev K V, Seyller T, Speck F, Ley L, Stojanov P, Riley J D and Leckey R G C 2007 *Mater. Sci. Forum* **556/557** 525
[126] Zhou S Y, Gweon G-H, Fedorov A V, First P N, de Heer W A, Lee D-H, Guinea F, Castro Neto A H and Lanzara A 2007 *Nat. Mater.* **6** 770
[127] Ohta T, Bostwick A, McChesney J L, Seller T, Horn K and Rotenberg E 2007 *Phys. Rev. Lett.* **98** 206802
[128] Mattausch A and Pankratov O 2007 *Phys. Rev. Lett.* **99** 076802
[129] Hass J, Varchon F, Millán-Otoya J E, Sprinkle M, Sharma N, de Heer W A, Berger C, First P N, Magaud L and Conrad E H 2008 *Phys. Rev. Lett.* **100** 125504
[130] Barrett N, Krasovskii E E, Themlin J-M and Strocov V N 2005 *Phys. Rev.* B **71** 035427
[131] Burdett J K 1995 *Chemical Bonding in Solids* (New York: Oxford University Press) p 152
[132] see references in Dresselhaus M S, Dresselhaus G, Sugihara K, Spain I L and Goldberg H A 1988 *Graphite Fibers and Filaments* (*Springer Series in Material Science* vol 5) (Berlin: Springer)
[133] Franklin R E 1951 *Acta Crystallogr.* **4** 253
[134] see Hutcheon J M 1970 *Modern Aspects of Graphite Technology* ed L C F Blackman (London: Academic)
[135] Kolmogorov A N and Crespi V H 2005 *Phys. Rev.* B **71** 235415
[136] Campanera J M, Savini G, Suarez-Martinez I and Heggie M I 2007 *Phys. Rev.* B **75** 235449
[137] -Tat Pong W and Durkan C 2005 *J. Phys. D: Appl. Phys.* **38** R329
[138] Robinson I K 1991 *Handbook on Synchrotron Radiation* vol 3, ed G S Brown and D E Moncton (Amsterdam: North-Holland) p 221
[139] Robinson I K 1986 *Phys. Rev.* B **33** 3830
[140] Jellison G E Jr, Hunn J D and Lee H N 2007 *Phys. Rev.* B **76** 85125
[141] Bauer E 1994 *Rep. Prog. Phys.* **57** 895
[142] Man K L, Qiu Z Q and Altman M S 2004 *Phys. Rev. Lett.* **93** 236104